INTERNATIONAL JOURNAL FOR NUMERICAL METHODS IN ENGINEERING
Int. J. Numer. Meth. Engng 2000; **48**:1285–1309

Numerical simulations of strain localization in inelastic solids using mesh-free methods

Shaofan Li*,† and Wing Kam Liu‡

Department of Mechanical Engineering, Northwestern University, 2145 Sheridan Road, Evanston, IL 60208, U.S.A.

SUMMARY

In this paper, a comprehensive account on using mesh-free methods to simulate strain localization in inelastic solids is presented. Using an explicit displacement-based formulation in mesh-free computations, high-resolution shear-band formations are obtained in both two-dimensional (2-D) and three-dimensional (3-D) simulations without recourse to any mixed formulation, discontinuous/incompatible element or special mesh design. The numerical solutions obtained here are insensitive to the orientation of the particle distributions if the local particle distribution is quasi-uniform, which, to a large extent, relieves the mesh alignment sensitivity that finite element methods suffer.

Moreover, a simple *h*-adaptivity procedure is implemented in the explicit calculation, and by utilizing a mesh-free hierarchical partition of unity a spectral (wavelet) adaptivity procedure is developed to seek high-resolution shear-band formations. Moreover, the phenomenon of multiple shear band and mode switching are observed in numerical computations with a relatively coarse particle distribution in contrast to the costly fine-scale finite element simulations. Copyright © 2000 John Wiley & Sons, Ltd.

KEY WORDS: *h*-adaptivity; hierarchical reproducing kernel partition of unity; mesh-free methods; strain localization; spectral adaptivity; wavelet kernel

1. INTRODUCTION

The numerical simulation of strain localization, or localized strong/weak discontinuous deformation field in inelastic solids has important engineering significances and applications, such as predicting failures of ductile materials.

The strain localization problem has been extensively studied over the past two decades, from the aspects of both constitutive modelling and numerical simulation (e.g. [1–3], Reference [3]

*Correspondence to: Shaofan Li, Department of Mechanical Engineering, Northwestern University, 2145 Sheridan Road, Evanston, IL 60208-3111, U.S.A.
†E-Mail: sf-li@nwu.edu
‡E-Mail: w-liu@nwu.edu

Contract/grant sponsor: Army Research Office
Contract/grant sponsor: National Science Foundation
Contract/grant sponsor: Army High Performance Computing Research Center, Department of the Army, Army Research Laboratory: contract/grant number: SDAAH04-95-2-003, DAAH04-95-C-0008

Received 26 January 1999
Revised 1 March 1999

is a survey from computational perspective). Nonetheless, some technical issues remain open, at least from computational standpoint. The phenomenological rate-independent plasticity theory does not have an intrinsic length scale, and it predicts the shear band with zero width; this not only conflicts with experiment observations, which one might accept as an approximation, or a setback of idealization of constitutive modellings, but also introduces the well-known mesh-dependent pathology in numerical simulations. It seems to us that the current trend is leaning towards to non-local, or strain gradient plasticity theories, and seeking physical justifications for them in the micromechanics framework. Nevertheless, some of the difficulties in numerical simulations, in our opinion, may be related to computational technology itself rather than to constitutive modelling, and these issues might exist in upcoming nano-scale plasticity models as well. The present work is motivated by seeking a robust computational strategy/algorithm for strain localization problems. The emphasis in this study is placed on explicit, large deformation computations.

In numerical simulations of shear-band formation in inelastic solids, there are two types of mesh sensitivities. The first type of mesh-dependent sensitivity appears in phenomenological rate-independent plasticity; it is due to the fact that the rate-independent plasticity theories admit the zero width singular surface solution, and hence the discrete Galerkin formulations with finite mesh size are unable to capture this weak discontinuous surface precisely. Mathematically speaking, the inception of shear bands corresponds to the loss of ellipticity of the governing partial differential equations, which leads to the illposedness of the mixed initial/boundary value problem, and hence results in the collapse of discrete computation, if the conventional Galerkin procedure is employed. To eliminate such a type of mesh sensitivity requires regularization of the continuum, or discrete system; the rate-dependent plasticity, the non-local, and strain gradient plasticity are three main regularization procedures used in computations. The second type of mesh-dependent sensitivity is the so-called mesh-alignment sensitivity. It is often referred to as the inability of a finite element (FE) mesh to resolve localized shearing at angles oblique to the element boundaries, which occurs in mesh-based numerical computations regardless of whether a continuum system is regularized or not [4].

Mesh-alignment sensitivity occurs, in our opinion, because the finite element mesh poses additional, unphysical constraints on spatial symmetry of the material under study. Even though it may be a very weak constraint, and may not be susceptible in conventional stress/strain evaluation under normal circumstances, it plays a significant role in simulating bifurcation solutions, because any small perturbation matters in this situation. For instance, in computations, the localized shear band tends to go along with edges of finite element boundaries, regardless of its physical plausibility. By the way, there is a general belief, which may be worth verifying, that these two mesh-dependent sensitivities might be related. The argument is as follows: if a continuum has a finite length scale, and the characteristic length of FE mesh is smaller than the length scale, then there will be no mesh sensitivity of any kind at all and if FE mesh size is larger than the intrinsic length scale of the material, both mesh sensitivities occur.

In contrast to finite element methods (FEM), mesh-free methods (e.g. [5–10]) possess some special qualities, which the mesh-based numerical methods generically lack. First, mesh-free methods tend to be more objective to the ‘mesh’ environment or particle distribution than finite element methods; precisely speaking, a quasi-uniform mesh-free particle distribution in a local region tends to attain isotropy, or maximum symmetry in its spatial orientation. Second, moving least-squares interpolant-based mesh-free shape functions are constructed by embedding a highly smooth window function, such that ‘the reproducing kernel interpolation’ is usually a higher-order polynomial approximation; it can support the purely displacement-based formulation without incurring

volumetric locking within a certain range of support size of the window function. This fact has been observed by several authors (e.g. [5, 11, 12]). Third, most meshless methods may be viewed as non-local approximations, meaning that the approximation is derived as the discretization of a convolution of a smooth kernel 'transformation':

$$\langle u(\mathbf{x})\rangle = \int_{\Omega_y} \mathscr{K}(\mathbf{x}-\mathbf{y})u(\mathbf{y})\,\mathrm{d}\Omega \approx \sum_{I=1}^{\mathrm{NP}} \mathscr{K}(\mathbf{x}-\mathbf{x}_I)u_I \Delta\mathbf{x}_I \tag{1}$$

Intuitively, this discrete 'non-locality' can be interpreted as that every point in the domain is covered by multiple shape functions, whereas FEM may be referred to as a local approximation, because each nodal point of a FE mesh is covered by only one shape function. In principle, it is also impossible to construct a convolution with continuous kernel function that is equivalent to a FE interpolation. Thus, meshless methods offer a numerical mechanism to smear, or to smooth any discontinuous fields, enabling them to become regularized concentration fields. These properties provide an effective remedy for the mesh alignment sensitivity that has long plagued the computation of strain localization.

The departure in this study is the use of mesh-free discretization in numerical simulation of shear band formations, which distinguishes the present approach from many other computational approaches on studying strain localization problems. In this paper, the following aspects of the problems are studied: (1) explicit displacement-based computations; (2) mesh-alignment sensitivity; (3) *h*-adaptivity/spectral adaptivity; (4) multiple shear band/mode switching; (5) and 3-D shear band simulation.

2. BASIC FORMULATIONS

2.1. Reproducing kernel hierarchical partition of unity

Currently, several different mesh-free methods have been used in computational mechanics, such as smoothed particle hydrodynamics (SPH) [13], element-free Galerkin (EFG) [5], reproducing kernel particle method (RKPM) [12, 14–16], *h-p* clouds [17], etc. The particular mesh-free method used in this numerical simulation is the latest version of reproducing kernel particle method (RKPM). A detailed presentation of the methodology can be found in Li and Liu [18]. For clarity, some of the technical ingredients of the method are outlined below.

By constructing a group of the kernel functions $\{\mathscr{K}^{[0]}(x), \mathscr{K}^{[1]}(x), \ldots, \mathscr{K}^{[\beta]}(x)\}$, one may form a reproducing/filtering representation

$$u^{\varrho}_{[\beta]}(x) = \bar{\mathscr{R}}^m_{\varrho} u(x) = \int_{\Omega} \mathscr{K}_{\varrho}(y-x)u(y)\,\mathrm{d}\Omega \tag{2}$$

where $\mathscr{K}_{\varrho}(x) = \sum_{\alpha=0}^{\beta} C_\alpha \mathscr{K}^{[\alpha]}_{\varrho}(x)$, $|\beta| = m$, $\mathscr{K}_{\varrho}(x) := \dfrac{1}{\rho^n}\mathscr{K}(x)$ and C_α are given constants. Two interpolation schemes may be formed

$$u^{\varrho}_{[\beta],h}(x) = \sum_{\ell=\Lambda} u_\ell \mathscr{K}_\ell(x) \tag{3}$$

or

$$u^{\rho}_{[\beta],h}(x) = \mathscr{R}^m_{\rho} u(x) = \sum_{\ell\in\Lambda} u^{[00]}_\ell \mathscr{K}^{[00]}_\ell(x) + \sum_{\ell\in\overset{\circ}{\Lambda}} \sum_{\alpha=1}^{\beta} u^{[\alpha]}_\ell \mathscr{K}^{[\alpha]}_\ell(x), \quad |\beta| \leqslant m \tag{4}$$

where

$$\Lambda = \{\ell | 1, 2, \ldots, \mathrm{NP}\}, \quad \overset{\circ}{\Lambda} \subset\subset \Lambda \tag{5}$$

$$\mathscr{K}_{\ell}^{[\alpha]}(x) := \mathbf{P}\left(\frac{x_{\ell} - x}{\varrho}\right) \mathbf{b}^{(\alpha)}(x) \phi_{\varrho}(x_{\ell} - x) \Delta V_{\ell} \tag{6}$$

and

$$\mathbf{M}\mathbf{b}^{(\alpha)}(x) = \mathbf{1}^{(\alpha)}, \quad \mathbf{1}^{(\alpha)} = \{\underbrace{0, \ldots, 0, 1}_{\alpha}, 0, \cdots, 0\}^{\mathrm{T}} \tag{7}$$

We refer to

$$\Psi := \{\mathscr{K}_{\ell}^{[0]}(x), \mathscr{K}_{\ell}^{[1]}(x), \ldots, \mathscr{K}_{\ell}^{[\beta]}(x)\}_{\ell \in \Lambda} \tag{8}$$

as *the hierarchical partition of unity*, and refer to $\{\mathscr{K}^{[\alpha]}(x)\}$, $\alpha \neq 0$, as *the pre-wavelets*, or simply wavelet functions. Note that $\{\mathscr{K}_{\ell}^{[0]}(x)\}$ is a *partition of unity*:

$$\sum_{\ell \in \Lambda} \mathscr{K}_{\ell}^{[0]}(x) = 1 \tag{9}$$

whereas $\{\mathscr{K}_{\ell}^{[\alpha]}(x)\}, \alpha \neq 0$ are the *partition of nullity*:

$$\sum_{\ell \in \Lambda} \mathscr{K}_{\ell}^{[\alpha]}(x) = 0 \tag{10}$$

Remark 2.1. (i) Equations (2)–(3) are mesh-free discretizations;
(ii) Equations (1)–(3) are non-local approximations;
(iii) The set (8) is at most a frame, not a basis in $L^2(\Omega)$;
(iv) Equation (2) is related to the so-called 'synchronized reproducing kernel interpolant', which is an ideal platform to numerically implement the strain-gradient plasticity theory, or non-local plasticity theory (see Chen and Wu [19]).

Example 2 (2-D bilinear shape function). Let $\alpha =$ (0,0), (1,0), (0,1), (1,1); and $x_{\ell} = (x_{1\ell}, x_{2\ell})$, $x = (x_1, x_2)$. The vectors $\mathbf{b}^{(\alpha)}(x)$ in (6) are determined by the moment equations

$$\begin{pmatrix} m_{00}^h & m_{10}^h & m_{01}^h & m_{11}^h \\ m_{10}^h & m_{20}^h & m_{11}^h & m_{21}^h \\ m_{01}^h & m_{11}^h & m_{02}^h & m_{12}^h \\ m_{11}^h & m_{21}^h & m_{12}^h & m_{22}^h \end{pmatrix} \begin{pmatrix} b_1^{(00)} \\ b_2^{(00)} \\ b_3^{(00)} \\ b_4^{(00)} \end{pmatrix} = \begin{pmatrix} 1 \\ 0 \\ 0 \\ 0 \end{pmatrix}$$

$$\begin{pmatrix} m_{00}^h & m_{10}^h & m_{01}^h & m_{11}^h \\ m_{10}^h & m_{20}^h & m_{11}^h & m_{21}^h \\ m_{01}^h & m_{11}^h & m_{02}^h & m_{12}^h \\ m_{11}^h & m_{21}^h & m_{12}^h & m_{22}^h \end{pmatrix} \begin{pmatrix} b_1^{(10)} \\ b_2^{(10)} \\ b_3^{(10)} \\ b_4^{(10)} \end{pmatrix} = \begin{pmatrix} 0 \\ 1 \\ 0 \\ 0 \end{pmatrix}$$

$$\begin{pmatrix} m^h_{00} & m^h_{10} & m^h_{01} & m^h_{11} \\ m^h_{10} & m^h_{20} & m^h_{11} & m^h_{21} \\ m^h_{01} & m^h_{11} & m^h_{02} & m^h_{12} \\ m^h_{11} & m^h_{21} & m^h_{12} & m^h_{22} \end{pmatrix} \begin{pmatrix} b_1^{(01)} \\ b_2^{(01)} \\ b_3^{(01)} \\ b_4^{(01)} \end{pmatrix} = \begin{pmatrix} 0 \\ 0 \\ 1 \\ 0 \end{pmatrix}$$

$$\begin{pmatrix} m^h_{00} & m^h_{10} & m^h_{01} & m^h_{11} \\ m^h_{10} & m^h_{20} & m^h_{11} & m^h_{21} \\ m^h_{01} & m^h_{11} & m^h_{02} & m^h_{12} \\ m^h_{11} & m^h_{21} & m^h_{12} & m^h_{22} \end{pmatrix} \begin{pmatrix} b_1^{(11)} \\ b_2^{(11)} \\ b_3^{(11)} \\ b_4^{(11)} \end{pmatrix} = \begin{pmatrix} 0 \\ 0 \\ 0 \\ 1 \end{pmatrix}$$

The kernel-functions constructed based on (6) are displayed in Plate 1.

Then, the zeroth order reproducing kernel interpolation, and higher-order reproducing kernel approximation can be put in the form

$$u^{\rho}_{[0]}(x) = \sum_{I \in \Lambda} u_I^{[0]} \Psi_I^{[0]}(x) \tag{11}$$

and the higher-order wavelet interpolation, in the form

$$u^{\rho}_{[\beta]}(x) = \sum_{I \in \Lambda} u_I^{[0]} \Psi_I^{[0]}(x) + \sum_{I \in \overset{\circ}{\Lambda}} \sum_{\alpha=1}^{\beta} u_I^{[\alpha]} \Psi_I^{[\alpha]}(x), \quad \beta = 1, 2, 3 \tag{12}$$

where $\{\Psi_I^{[0]}(x)\}$ is the basis of the zeroth-order kernel function, and $\{\Psi_I^{[\alpha]}(x)\}$, $\alpha \neq 0$, are the wavelet-like basis.

2.2. An explicit mesh-free Galerkin formulation

Because of its simplicity, explicit computation is very attractive in practical computations, especially for large-scale computations of large deformation problems. However, most inelastic materials are nearly incompressible, which poses some technical difficulties in displacement-based finite element simulations. To be more specific, the displacement-based Galerkin formulation may induce volumetric locking, which leads to computational failure. In practice, such difficulty is usually handled by either mixed formulations, for instance the incompatible element or enhanced strain methods (e.g. [20]), or some *ad hoc* treatments, such as one-point (1-pt) integration/hour-glass control procedure, and selective reduced integration scheme (e.g. the B-bar element proposed by Hughes [21]). Furthermore, to capture strain localizations in inelastic materials, one may have to develop special discontinuous incompatible element, which, to some extent, complicates the implementation since they are usually not suitable for explicit computations. For example, an immediate difficulty is how to adapt the mixed formulations for a quadrilateral (or hexahedral) grid. One of the few options available is to use 1-pt integration with hour-glass control scheme [22]. However, this leads to other problems as well. For instance, the actual shear-band mode may consist of some hour-glass modes; thus, the suppression of the hour-glass mode while retaining the correct shear-band mode is entirely based on trial and error. Particularly, for the power-law-governed elasto-viscoplastic solids, it has been found in a recent study by Watanabe *et al*. [23] that it may

be difficult to suppress hour-glass modes for large power index, m. Besides these drawbacks, there is a major difficulty for explicit finite element algorithm to proceed with h-adaptive refinement, while keeping the quadrilateral (or hexahedral) pattern intact. To remedy the inadequacy of finite element methods, a mesh-free explicit formulation is proposed.

Consider the equation of motion

$$\sigma_{ji,j} + b_i = \rho \dot{v}_i \tag{13}$$

where $\boldsymbol{\sigma}$ is the Cauchy stress, $\mathbf{b}$ is the body force per unit volume, ρ is the density of the material and $\mathbf{v}$ is the velocity of the continuum. For simplicity, the boundary conditions are specified with respect to the referential configuration

$$\mathbf{P}\mathbf{n}_0 = \mathbf{T}^0, \quad \forall \mathbf{X} \in \Gamma_X^T \tag{14}$$

$$\mathbf{u} = \mathbf{u}^0, \quad \forall \mathbf{X} \in \Gamma_X^u \tag{15}$$

where $\mathbf{P}$ is the first Piola–Kirchhoff stress tensor, and $\Gamma_X^T \cup \Gamma_X^u = \partial\Omega_X$.

Consider a weighted residual form of (13):

$$\int_{\Omega_x} \{\rho \ddot{u}_i - \sigma_{ji,j} - b_i\} \delta u_i \, \mathrm{d}\Omega_x = 0 \tag{16}$$

Then the following weak form can be derived:

$$\int_{\Omega_X} \rho_0 \ddot{u}_i \delta u_i \, \mathrm{d}\Omega_X + \int_{\Omega_X} P_{Ji} \delta F_{Ji}^T \, \mathrm{d}\Omega_X - \int_{\Omega_X} B_i \delta u_i \, \mathrm{d}\Omega_X - \int_{\Gamma_X^T} T_i^0 \delta u_i \, \mathrm{d}\Gamma - \int_{\Gamma_X^u} T_i \delta u_i \, \mathrm{d}\Gamma = 0 \tag{17}$$

Assume that the discrete trial, and weighting functions have the form

$$u_i^h(\mathbf{X}, t) = \sum_{I=1}^{\mathrm{NP}} N_I(\mathbf{X}) d_{iI}(t) \tag{18}$$

$$\delta u_i^h(\mathbf{X}, t) = \sum_{I=1}^{\mathrm{NP}} N_I(\mathbf{X}) \delta d_{iI}(t) \tag{19}$$

Unlike FE approximation, the RKPM interpolant has a drawback: its inability to represent essential boundary condition via boundary value interpolation, i.e.

$$u_i^h(\mathbf{X}, t) \neq u_i^0(\mathbf{X}, t), \quad \forall \mathbf{X} \in \Gamma^u \tag{20}$$

This is reflected in the weak form (17) as the extra term, $\int_{\Gamma_X^u} T_i \delta u_i \, \mathrm{d}\Gamma$, which is a nuisance because the traction force, T_i, is unknown on the essential boundary. Before proceeding further, we have to modify the mesh-free interpolant such that the essential boundary conditions are taken into account in the interpolation scheme. To do this, we distribute N_b number of particles on the boundary Γ^u,

and impose certain conditions on the mesh-free interpolant, $u^h(\mathbf{X},t) \in \text{span}\{N_I(\mathbf{X}) \mid I = 1,\ldots,\text{NP}\}$, such that

$$u_i^h(\mathbf{X}_I,t) = u_i^0(\mathbf{X}_I,t) =: g_i(\mathbf{X}_I,t), \quad I = 1,\ldots,N_b \tag{21}$$

For simplicity, we denote $g_{iI}(t) := g_i(\mathbf{X}_I,t), \quad I = 1,\ldots,N_b$. Let $N_{nb} := \text{NP} - N_b$. The particles and the associated discrete field variables can be separated into two groups, each of which are marked with superscript b and nb respectively:

$$\begin{aligned} u_i^h(\mathbf{X},t) &= \sum_{I=1}^{\text{NP}} N_I(\mathbf{X}) d_{iI}(t) = \sum_{I=1}^{N_b} N_I^b(\mathbf{X}) d_{iI}^b(t) + \sum_{I=1}^{N_{nb}} N_I^{nb}(\mathbf{X}) d_{iI}^{nb}(t) \\ &= \mathbf{N}^b(\mathbf{X})\mathbf{d}_i^b(t) + \mathbf{N}^{nb}(\mathbf{X})\mathbf{d}_i^{nb}(t) \end{aligned} \tag{22}$$

where

$$\mathbf{N}^b(\mathbf{X}) := \{N_1^b(\mathbf{X}),\ldots,N_{N_b}^b(\mathbf{X})\}, \qquad \mathbf{d}_i^b(t) := \{d_{i1}^b(t),\ldots,d_{iN_b}^b(t)\} \tag{23}$$

$$\mathbf{N}^{nb}(\mathbf{X}) := \{N_1^{nb}(\mathbf{X}),\ldots,N_{N_{nb}}^{nb}(\mathbf{X})\}, \quad \mathbf{d}_i^{nb}(t) := \{d_{i1}^{nb}(t),\ldots,d_{iN_{nb}}^{nb}(t)\} \tag{24}$$

Let

$$\mathbf{D}^b := \begin{pmatrix} & \vdots & \\ \cdots & N_I^b(\mathbf{X}_J) & \cdots \\ & \vdots & \end{pmatrix}^{N_b \times N_b} \tag{25}$$

$$\mathbf{D}^{nb} := \begin{pmatrix} & \vdots & \\ \cdots & N_I^{nb}(\mathbf{X}_J) & \cdots \\ & \vdots & \end{pmatrix}^{N_b \times N_{nb}} \tag{26}$$

Thus the enforced discrete essential conditions, (21), may read as follows:

$$\mathbf{D}^b\mathbf{d}_i^b(t) = \mathbf{g}_i(t) - \mathbf{D}^{nb}\mathbf{d}_i^{nb}(t) \tag{27}$$

$$\mathbf{D}^b\delta\mathbf{d}_i^b(t) = -\mathbf{D}^{nb}\delta\mathbf{d}_i^{nb}(t) \tag{28}$$

where $\mathbf{g}_i(t) = \{g_i(\mathbf{X}_I,t)\}, \ I = 1,\ldots,N_b$.

After inverting matrix $\mathbf{D}^b$, one has

$$\mathbf{d}_i^b(t) = (\mathbf{D}^b)^{-1}\mathbf{g}_i(t) - (\mathbf{D}^b)^{-1}\mathbf{D}^{nb}\mathbf{d}_i^{nb}(t) \tag{29}$$

$$\delta\mathbf{d}_i^b(t) = -(\mathbf{D}^b)^{-1}\mathbf{D}^{nb}\delta\mathbf{d}_i^{nb}(t) \tag{30}$$

Substituting (29) back into (22) yields

$$u_i^h(\mathbf{X},t)=\sum_{I=1}^{\mathrm{NP}} N_I(\mathbf{X})d_{iI}(t)=\mathbf{N}^b(\mathbf{X})(\mathbf{D}^b)^{-1}\mathbf{g}_i(t) + (\mathbf{N}^{nb}(\mathbf{X})-\mathbf{N}^b(\mathbf{X})(\mathbf{D}^b)^{-1}\mathbf{D}^{nb})\mathbf{d}_i^{nb}(t) \tag{31}$$

$$\delta u_i^h(\mathbf{X},t)=(\mathbf{N}^{nb}(\mathbf{X})-\mathbf{N}^b(\mathbf{X})(\mathbf{D}^b)^{-1}\mathbf{D}^{nb})\delta\mathbf{d}_i^{nb}(t) \tag{32}$$

Obviously, for $\mathbf{X}_I\in\Gamma^u$, $I=1,\ldots,N_b$

$$u_i^h(\mathbf{X}_I,t)=g_{iI}(t) \tag{33}$$

$$\delta u_i^h(\mathbf{X}_I,t)=0,\quad I=1,2,\ldots,N_b \tag{34}$$

Equation (31) can also be interpreted as the transformation of shape functions, i.e.

$$u_i^h(\mathbf{X},t)=\sum_{I=1}^{N_b} W_I^b(\mathbf{X})u_{iI}(t)+\sum_{I=1}^{N_{nb}} W_I^{nb}(\mathbf{X})d_{iI}(t)=\mathbf{W}^b(\mathbf{X})\mathbf{u}_i^0(t)+\mathbf{W}^{nb}(\mathbf{X})\mathbf{d}_i^{nb}(t) \tag{35}$$

where $\mathbf{W}^b(\mathbf{X}):=\mathbf{N}^b(\mathbf{X})(\mathbf{D}^b)^{-1}$, and $\mathbf{W}^{nb}(\mathbf{X}):=[\mathbf{N}^{nb}(\mathbf{X})-\mathbf{N}^b(\mathbf{X})(\mathbf{D}^b)^{-1}\mathbf{D}^{\mathrm{nb}}]$. One may notice that the new shape functions in (35) at essential boundary possess the Kronecker delta, or interpolation property.

To this end, only a set of discrete number points, N_b, satisfy the essential boundary condition. However, based on (32), we claim that

$$\int_{\Gamma^u} T^i\delta u_i^h\,\mathrm{d}\Gamma=\int_{\Gamma^u} T^i(\mathbf{X},t)\{\mathbf{N}^{nb}(\mathbf{X})-\mathbf{N}^b(\mathbf{X})(\mathbf{D}^b)^{-1}\mathbf{D}^{nb}\}\delta\mathbf{d}_i^{nb}(t)\,\mathrm{d}\Gamma\approx 0 \tag{36}$$

In 2-D case, this fact can be made clear by considering a special case. Assume that the essential boundary is a straight line segment $[a,b]$, and there are N_b particles distributed evenly on the segment. For fixed t, let

$$f_i(\mathbf{X})=(\mathbf{N}^{nb}(\mathbf{X})-\mathbf{N}^b(\mathbf{X})(\mathbf{D}^b)^{-1}\mathbf{D}^{nb})\cdot\delta\mathbf{d}_i^{nb} \tag{37}$$

Then each of the three scalar functions, $f_i(\mathbf{X})$, has N_b points that have zero values along the boundary segment $[a,b]$. This is because

$$\mathbf{N}^b(\mathbf{X}_I)(\mathbf{D}^b)^{-1}=(\underbrace{0,\ldots,0,1}_{I},0,\ldots,0) \tag{38}$$

$$(\underbrace{0,\ldots,0,1}_{I},0,\ldots,0)\mathbf{D}^{nb}=\mathbf{N}^{nb}(\mathbf{X}_I),\quad I=1,2,\ldots,N_b \tag{39}$$

Consequently

$$(\mathbf{N}^{nb}(\mathbf{X}_I)-\mathbf{N}^b(\mathbf{X}_I)(\mathbf{D}^b)^{-1}\mathbf{D}^{nb})=(0,0,\ldots,0),\quad I=1,2,\ldots,N_b \tag{40}$$

Based on the trapezoidal rule, or the Simpson rule, the following estimate can be reached immediately:

$$\left|\int_{\Gamma^u} T^i \delta u_i^h \, \mathrm{d}\Gamma\right| \leqslant \begin{cases} \sup\limits_{X\in[a,b]} \{\left|T^i(X,t)\right|\} \dfrac{(b-a)h^2}{12} \left|f_i^{(2)}(\zeta)\right|, & a<\zeta<b \\ \sup\limits_{X\in[a,b]} \{\left|T^i(X,t)\right|\} \dfrac{(b-a)h^4}{180} \left|f_i^{(4)}(\zeta)\right|, & a<\zeta<b \end{cases} \tag{41}$$

This is because we deliberately choose the sample points of the trapezoidal rule, or the Simpson rule as those points at which the essential boundary condition is enforced. Thus at every sampling point, $\mathbf{X}_I$, $I=1,2,\ldots,N_b$, $f_i(\mathbf{X}_I)=0$, and therefore the discrete summation $\sum_I f_I w_I = 0$; here w_I are the integration weight. Note that $h := (b-a)/N_b$. This estimate can be further improved, provided that the window function is 'very smooth'. In other words, Equation (41) suggests that if the window function is sufficiently smooth, the error coming from the approximated essential boundary condition (33) can be made the same, or even less than the interpolation error; this proves our claim.

Substitute the modified reproducing kernel interpolant,

$$u_i^h(\mathbf{X},t) = \sum_{I=1}^{\mathrm{NP}} N_I(\mathbf{X}) d_{iI}(t) \tag{42}$$

as both trial and weighting functions into the weak formulation. The discrete equations of motion can be put into the standard form,

$$\mathbf{M}\ddot{\mathbf{d}} + \mathbf{f}^{\mathrm{int}} = \mathbf{f}^{\mathrm{ext}} \tag{43}$$

where $\mathbf{M}$ is the mass matrix, and

$$\mathbf{f}_I^{\mathrm{ext}} = \int_{\Gamma_X^T} T_i^0(\mathbf{X},t) N_I(\mathbf{X}) \mathbf{e}_i \, \mathrm{d}\Gamma + \int_{\Omega_X} B_i(\mathbf{X},t) N_I(\mathbf{X}) \mathbf{e}_i \, \mathrm{d}\Omega \tag{44}$$

$$\mathbf{f}_I^{\mathrm{int}} = \int_{\Omega_X} P_{Ji} \frac{\partial N_I}{\partial X_J} \mathbf{e}_i \, \mathrm{d}\Omega \tag{45}$$

In computation, an elasto-visco-plasticity material is used as constitutive model, which is described in the appendix. A forward gradient time integration scheme—the rate tangent modulus method by Peirce *et al.* [24] is adapted as the time integrator for constitutive update, and the conventional predictor–corrector scheme is used to update the deformation. The only difference between the mesh-free explicit scheme and the conventional FEM explicit scheme is that in each time iteration one has to enforce, or to update the essential boundary conditions:

$$\mathbf{d}_i^b(t) = (\mathbf{D}^b)^{-1}(\mathbf{g}_i(t) - \mathbf{D}^{nb}\mathbf{d}_i^{nb}(t)) \tag{46}$$

$$\dot{\mathbf{d}}_i^b(t) = (\mathbf{D}^b)^{-1}(\dot{\mathbf{g}}_i(t) - \mathbf{D}^{nb}\dot{\mathbf{d}}_i^{nb}(t)) \tag{47}$$

The essential boundary condition enforcement is accurate, only if there are enough particles distributed along the essential boundary.

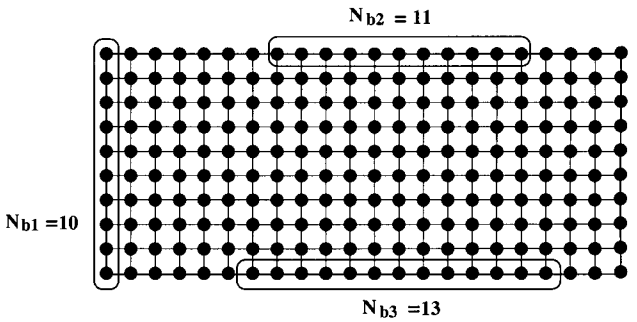

Figure 1. Piecewise essential boundaries.

Remark 2.2. (1) The ability of reproducing kernel shape functions to avoid locking in a displacement-based formulation is due to the following reasons:

(i) *It is a higher-order polynomial interpolation.* In Example 2, the embedded window function is a 2-D cubic spline box function, and the kernel function is constructed by multiplying an additional bilinear polynomial basis;

(ii) The use of sub-reduced integration scheme. All the calculations in this paper have been done, unless specified otherwise, by using 2×2 Gauss quadrature integration in 2-D, and $2 \times 2 \times 2$ Gauss quadrature integration in 3-D; they are still reduced integration schemes in principle; however, it appears that neither hour-glass mode, nor zero-energy mode occurs under such sub-reduced integration scheme.

(2) Equations (46) and (47) are a local essential boundary enforcement. In this setting, no global transformation is needed as proposed by Chen *et al.* [25]. One can enforce the essential boundary conditions piece by piece to avoid inverting large algebraic matrix, as illustrated in Figure 1.

3. MESH-ALIGNMENT SENSITIVITY

3.1. Model problems

The model problems considered in this paper are tension and compression tests of elasto-viscoplastic specimens under either plane strain, or three-dimensional loading conditions. For plane strain problem, the prescribed displacement/velocity boundary condition is imposed at both ends of the specimens as shown in Figure 2. Numerical results obtained from tension test and compression test under the plane strain condition are displayed in Plates 2 and 3.

3.2. Mesh-alignment sensitivity

In fact, mesh-alignment sensitivity would be the first difficulty to encounter, if anyone wishes to use FEM to simulate shear-band formations. In the early study [2], Tvergaard *et al.* used the classic quadrilateral element (CST4), which consists of four diagonally crossed constant strain triangle elements, to simulate shear-band formations under plane strain condition. CST4 element was originally designed by Nagategal *et al.* [26] to be used in a displacement-based formulation to avoid locking for computations in elasto-plastic materials. In their work [2], Tvergaard *et al.* made

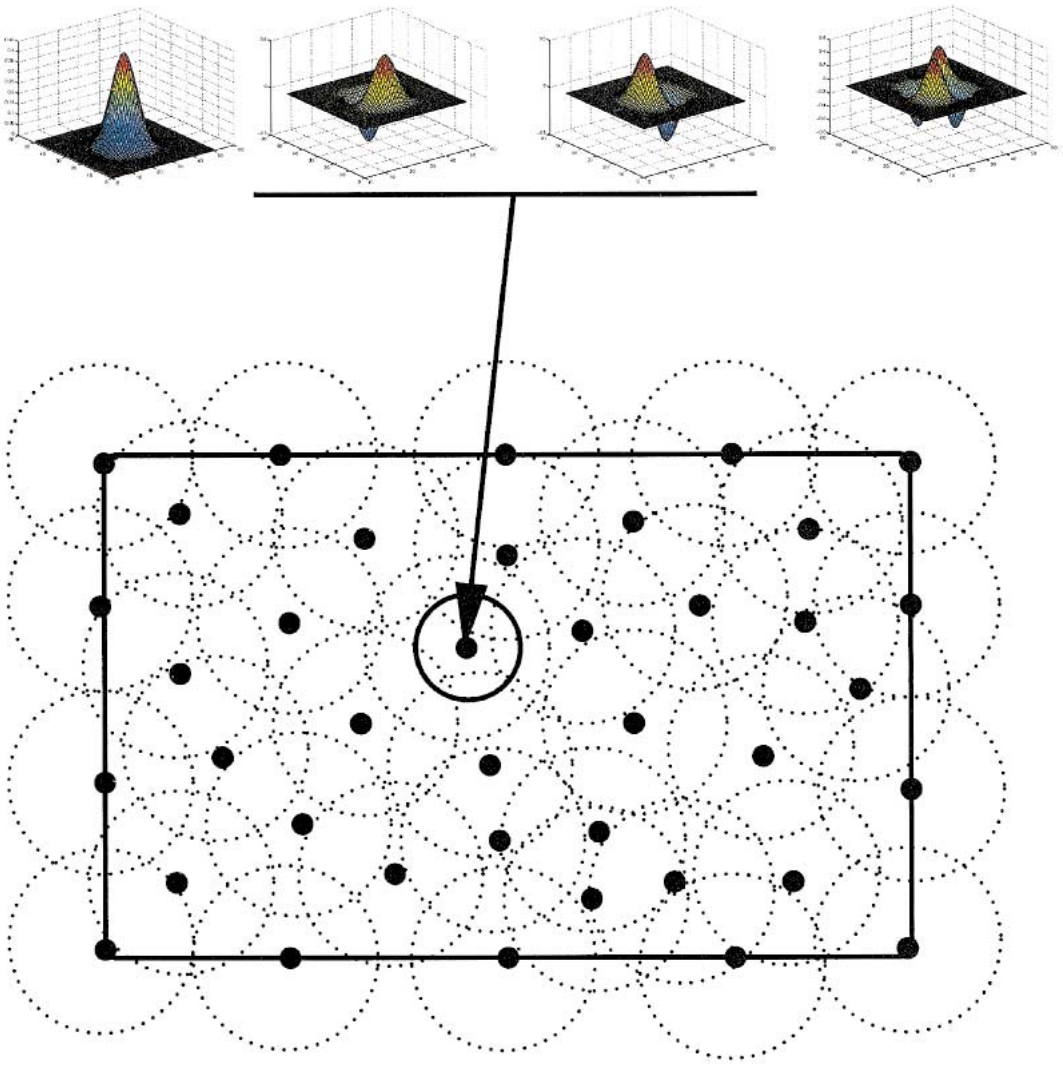

Plate 1. Two-dimensional meshfree hierarchical partition of unity generated by the bilinear polynomial basis, $\mathbf{P} = (1, x_1, x_2, x_1x_2)$: (1) $\alpha = (0, 0)$, (2) $\alpha = (1, 0)$, (3) $\alpha = (0, 1)$, (4) $\alpha = (1, 1)$

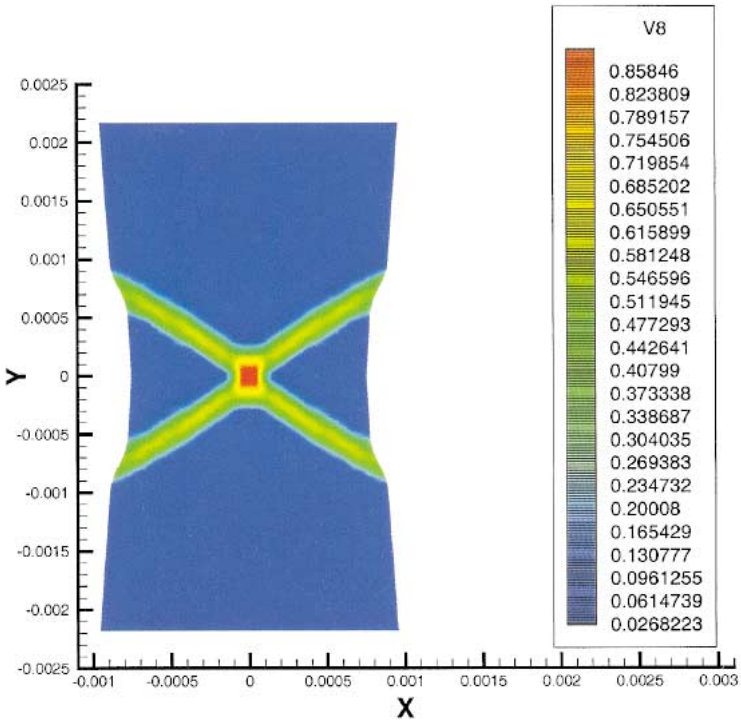

Plate 2. The contours of the effective viscoplastic strain in the tensile bar.

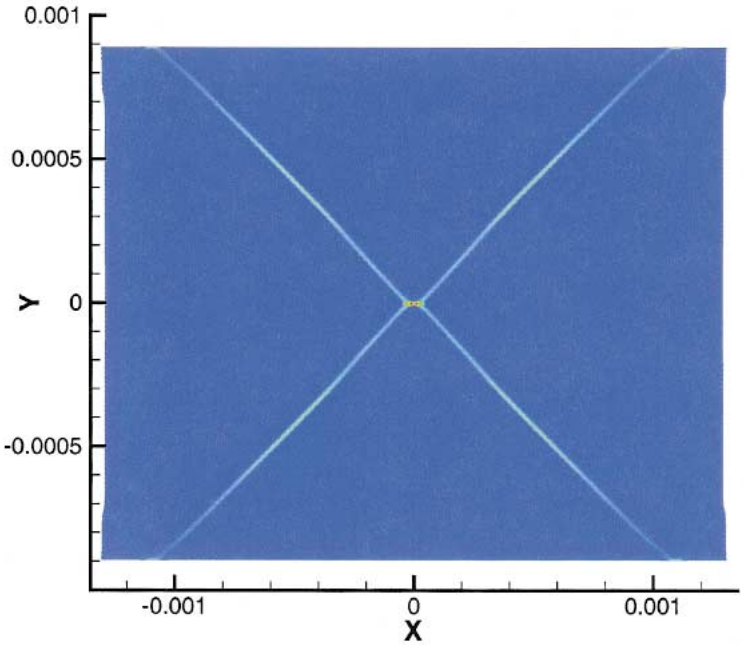

Plate 3. The contours of the effective viscoplastic strain in a slab under the compression test (r_0 = 0.1 mm).

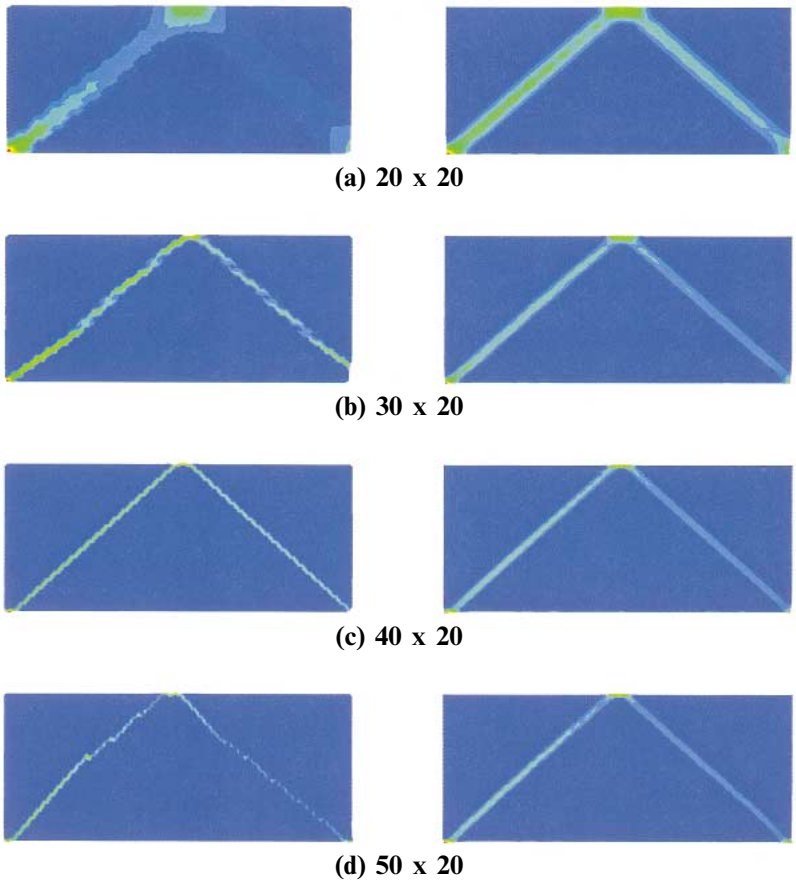

Plate 4. Comparison between FEM and RKPM with different aspect ratios in mesh/particle distribution.

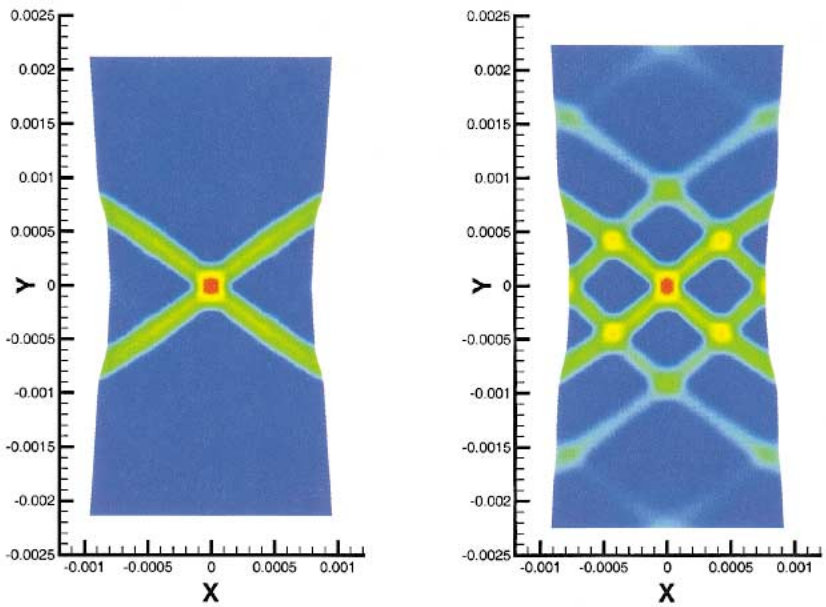

Plate 5. The comparison between the results based on normal lumped mass and special lumped mass techniques.

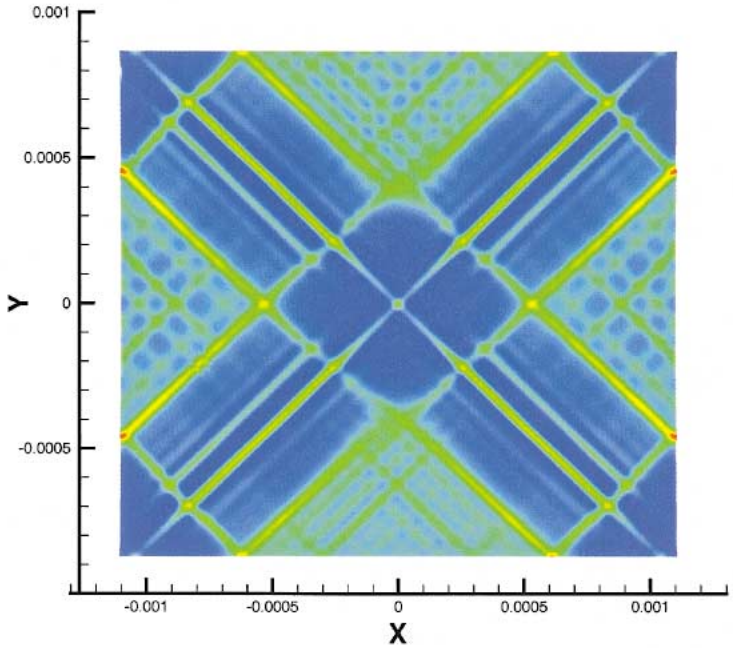

Plate 6. The high resolution shear-band solution obtained by special lumping technique.

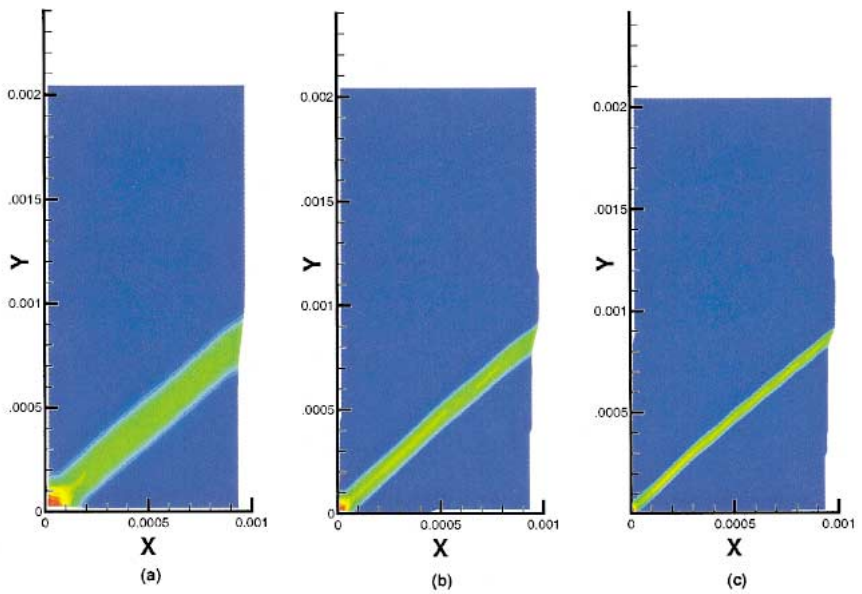

Plate 7. The contours of the effective viscoplastic strain in the tensile bar (only a quartern specimen shown): (a) without any adaptivity; (b) the first level adaptive solution; and (c) the second level adaptive solution.

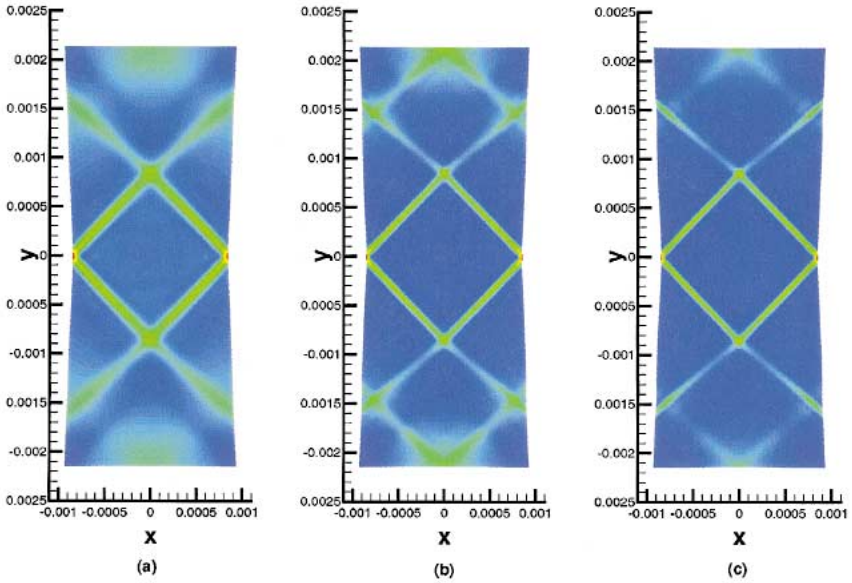

Plate 8. The contours of the effective viscoplastic strain in the tensile bar: (a) without wavelet adaptivity; (b) with wavelet adaptivity (α = (1, 0), (0, 1)); and (c) with wavelet adaptivity (α = (1, 0), (0, 1), (1, 1)).

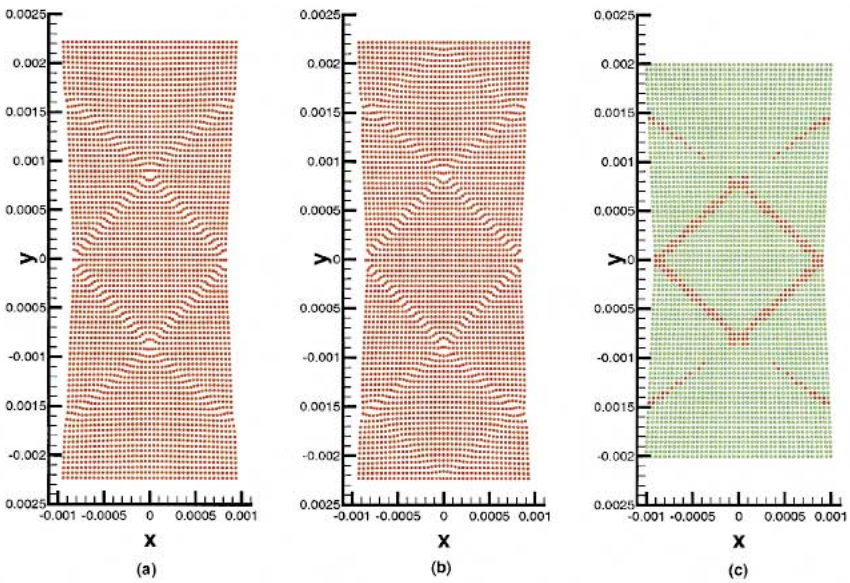

Plate 9. The shear-band in the tensile bar represented by particle formation: (a) without wavelet adaptivity; (b) with wavelet adaptivity; and (c) the adaptivity pattern in undeformed configuration.

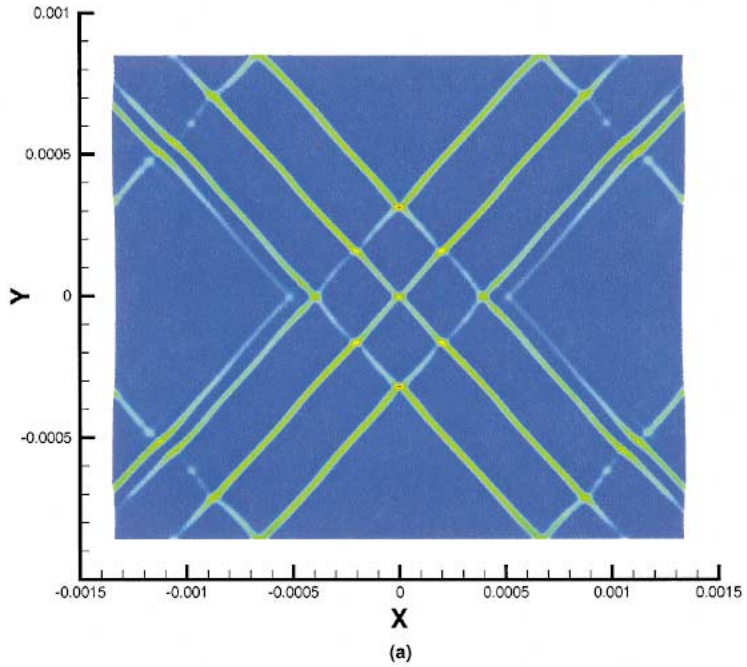

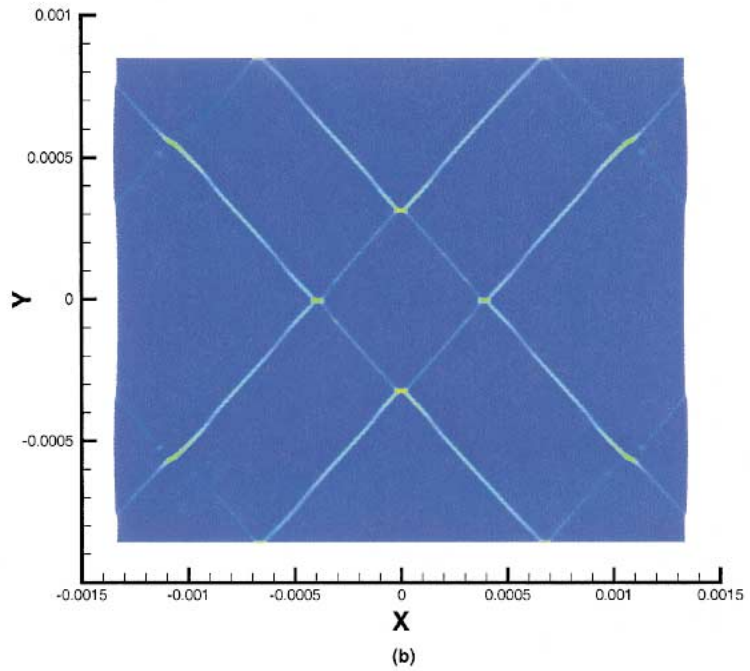

Plate 10. Multiple shear-bands in elasto-viscoplastic materials with different magnitude of imperfections: (a) $r_0 = 0.0041$ mm; and (b) $r_0 = 0.003$ mm.

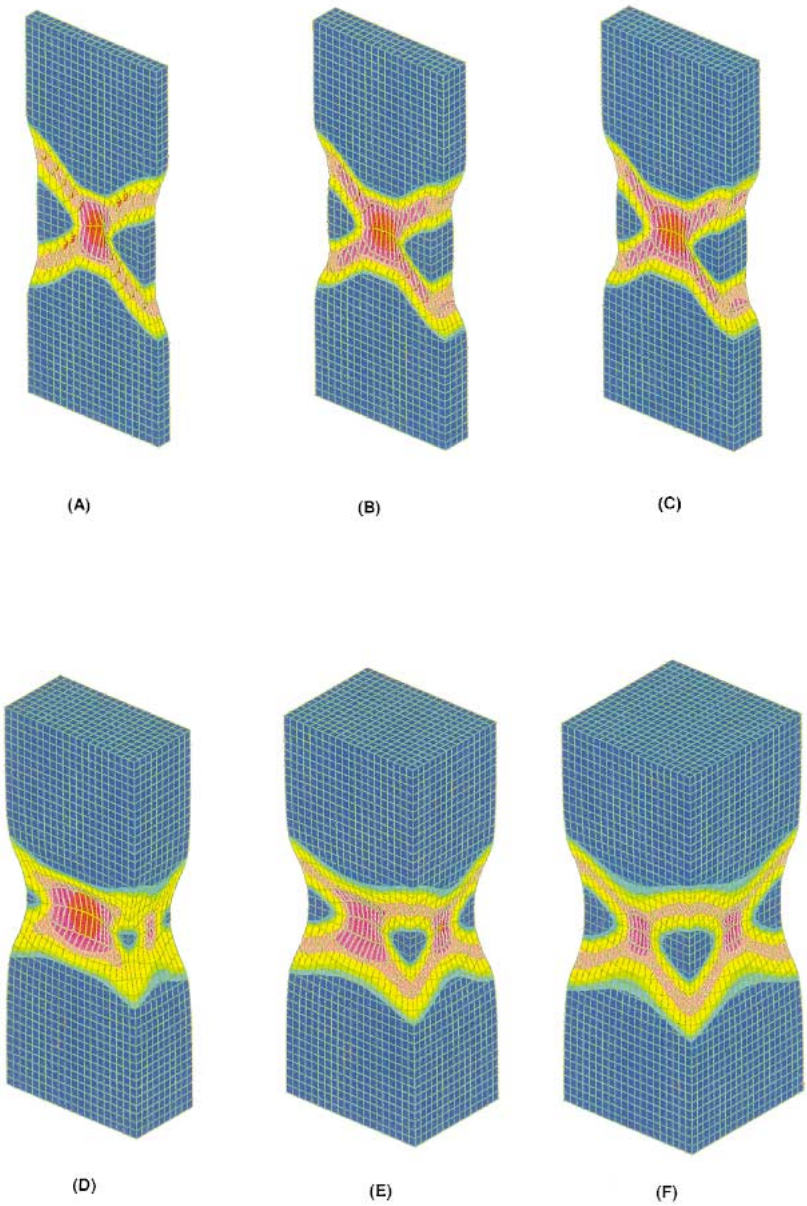

Plate 11. The contours of effective viscoplastic strain on three-dimensional tension specimens with different aspect ratios between width and thickness: (a) $t/W = 1/10$; (b) $t/W = 1/5$; (c) $t/W = 1/4$; (d) $t/W = 1/2$; (e) $t/W = 3/4$; (f) $t/W = 1/1$.

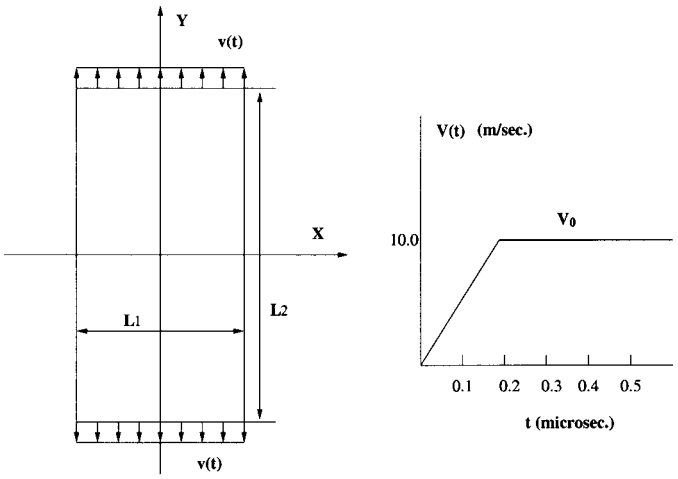

Figure 2. Model Problem: tension test ($v(t)>0$); compression test ($v(t)<0$).

an optimal arrangement of the aspect ratio of CST4 element, such that the shear-band formations are aligned with the boundary of finite elements, and sharp shear-bands are accurately captured in the computation. Few years later, following the same philosophy, Tvergaard [27] invented a box-shaped super-element (BST24) consisting of 24 tetrahedral element to compute the shear-band formation in three-dimensional (3-D) space. Both CST4 and BST24 elements show strong mesh-alignment sensitivity, which means that when shear-band orientation is oblique to the diagonal line or plane of the quadrilateral/hexahedral element, the computational results deteriorate. Thus, special mesh design is needed to align the finite element boundary properly along the shear-band orientation *a priori*.

To overcome the limitations of CST4/BST24 element, special elements have been considered and designed to relieve locking and offset the undesirable mesh-alignment sensitivity, though sometimes it is difficult to achieve both ends at the same time. These special elements usually fall into the following categories:

(i) *QR4-element*: That is, the four nodes quadrilateral with 1-pt integration/hour-glass control, which was first used in shear-band calculation by Nemat-Nasser *et al.* [22]. The 3-D counterpart of QR4-element is the brick element (BR8) with 1-pt/hour-glass control, which was first used by Zbib *et al.* [28] in 3-D shear-band calculation.
(ii) *QLOC-element* [29] QLOC-element and its derivatives, such as QS [30], and the regularized discontinuous element [31].

In practical computations, all these elements have pros and cons. The QR4/BR8 class element has the best overall performance, but it is difficult to make any *h*-type refinement, because any valid *h*-adaptivity will destroy the simple structure of QR4/BR8 elements. Moreover, unlike some other numerical computations, the strain localization modes often contain hour-glass modes; in other words, hour-glass modes are not independent of strain localization modes; usually the choice of artificial damping force is completely based on either empirical experiences, or plausible argument, which is at the expense of sacrifice any hope for an accurate prediction on the shear-band formation

in post-bifurcation region. The QLOC-type elements are specially designed to eliminate mesh alignment sensitivity for arbitrary mesh arrangement, and they are theoretically sound and suitable for mixed formulations; but they are complicated to implement, apart from the fact that usually they are required to locate the incipient shear-band position, or the strong/weak discontinuous line/surfaces *a priori*. In general, it is difficult to use them if the singular line/surface has non-zero curvature, or if one deals with complicate shear-band patterns, such as the micro-shear-band and macro-shear-band interaction in crystal plasticity. Therefore, the available remedies for mesh-alignment sensitivity, in our opinion, are either too complex to use, or too *ad hoc* and severely limited for a user in general purposes.

In principle, one may think that the mesh structure constraint is a numerical artifact that is coerced subjectively onto the deformed continuum, which might be more than necessary as the physically required compatibility condition of the solid. On the contrary, mesh-free methods, which do not have any definite mesh structure, may be free from such mesh-alignment constraints. Based on this intuitive notion, numerical experiments have been conducted to test this hypothesis. In a comparison study, a velocity boundary conditions is prescribed on both top/bottom surface of a slab, and an imperfection is planted as the reduction of yield stress at the lower left corner the specimen. The computations have been carried out using both CST4-element, and RKPM shape function at the same specimen with different aspect ratios of element size or size of background cell. The FEM and RKPM results are juxtaposed in Plate 4. One can find that comparing with the results obtained using CST4-element, the shear-band results obtained by using RKPM shape function always have the same, and correct orientation regardless of the aspect ratio of background cells.

4. NEW TECHNIQUES

4.1. A mesh-free hour-glass control strategy

As mentioned above, QR4-element is the only viable option in explicit codes for shear-band computations, and it appears to be the most popular choice used in practice (e.g. [32, 22, 28]), because of its simplicity. One of the shortcomings of the scheme is how to choose a suitable hour-glass control scheme to suppress the hour-glass modes, while retaining the correct shear-band mode, because shear-band mode may consist of certain of hour-glass modes as well [22]. In fact, it has been pointed out in [22] that constitutive model itself may stimulate spurious deformation and the values of the hour-glass control parameters begin to affect the numerical results, once the deformation becomes unstable. It would be interesting to compare the mesh-free wavelet modes presented in Section 2 and hour-glass modes due to under integration. The mesh-free wavelet modes in Example 2 can be expressed as

$$\sum_{I\in\Lambda} \mathscr{K}_I^{[10]}(x_I - x) = 0 \tag{48}$$

$$\sum_{I\in\Lambda} (x_{1I} - x_1)\mathscr{K}_I^{[10]}(x_I - x) = 1 \tag{49}$$

$$\sum_{I\in\Lambda} (x_{2I} - x_2)\mathscr{K}_I^{[10]}(x_I - x) = 0 \tag{50}$$

$$\sum_{I\in\Lambda}(x_{1I}-x_1)(x_{2I}-x_2)\mathscr{K}_I^{[10]}(x_I-x)=0 \tag{51}$$

$$\sum_{I\in\Lambda}\mathscr{K}_I^{[01]}(x_I-x)=0 \tag{52}$$

$$\sum_{I\in\Lambda}(x_{1I}-x_1)\mathscr{K}_I^{[01]}(x_I-x)=0 \tag{53}$$

$$\sum_{I\in\Lambda}(x_{2I}-x_2)\mathscr{K}_I^{[01]}(x_I-x)=1 \tag{54}$$

$$\sum_{I\in\Lambda}(x_{1I}-x_1)(x_{2I}-x_2)\mathscr{K}_I^{[01]}(x_I-x)=0 \tag{55}$$

$$\sum_{I\in\Lambda}\mathscr{K}_I^{[11]}(x_I-x)=0 \tag{56}$$

$$\sum_{I\in\Lambda}(x_{1I}-x_1)\mathscr{K}_I^{[11]}(x_I-x)=0 \tag{57}$$

$$\sum_{I\in\Lambda}(x_{2I}-x_2)\mathscr{K}_I^{[11]}(x_I-x)=0 \tag{58}$$

$$\sum_{I\in\Lambda}(x_{1I}-x_1)(x_{2I}-x_2)\mathscr{K}_I^{[01]}(x_I-x)=1 \tag{59}$$

whereas hour-glass mode in a four-node quadrilateral element can be represented by the mode shape function, $H_I(x)$ (see [33]), which satisfies the following conditions:

$$\sum_{I\in\Lambda_e}H_I(x_I-x)=0 \tag{60}$$

$$\sum_{I\in\Lambda_e}(x_{1I}-x_1)H_I(x_I-x)=0 \tag{61}$$

$$\sum_{I\in\Lambda_e}(x_{2I}-x_2)H_I(x_I-x)=0 \tag{62}$$

$$\sum_{I\in\Lambda_e}H_I^2(x_I-x)=4 \tag{63}$$

where Λ_e is the nodal index set in an element. It is clear that the hour-glass mode is also a *partition of nullity*, and it can be viewed as a special *wavelet* function as well, provided that the hour-glass modes are also compact supported. It, then, suggests that not all hour-glass modes are hazardous, and, as we speculate, non-zero energy modes may only furnish a 'complete' basis in the discrete functional space for elliptic type of partial differential equations (PDEs), but not for hyperbolic, parabolic as well as mixed type PDEs; in other words, the non-trivial zero-energy modes may carry some useful information for non-elliptic PDEs. Thus, the use of viscous force to suppress all the hour-glass modes without discretion can lead to potential errors in numerical simulations. In contrast to FEM, the 1-pt integration technique can still be used in reproducing kernel particle method without invoking artificial damping, or artificial stiffness. Precisely speaking, the undesirable hour-glass modes may be removed, or suppressed by properly adjusting the support size of the shape function, or dilation parameters of the window function, instead of imposing external viscous forces or modifying stiffness matrix. By doing so, one may be able to preserve the accuracy of the post-bifurcated shear band solutions without the pollution caused by the artificial hour-glass control. In Figure 3, a series of shear-band formations is displayed in a quarter

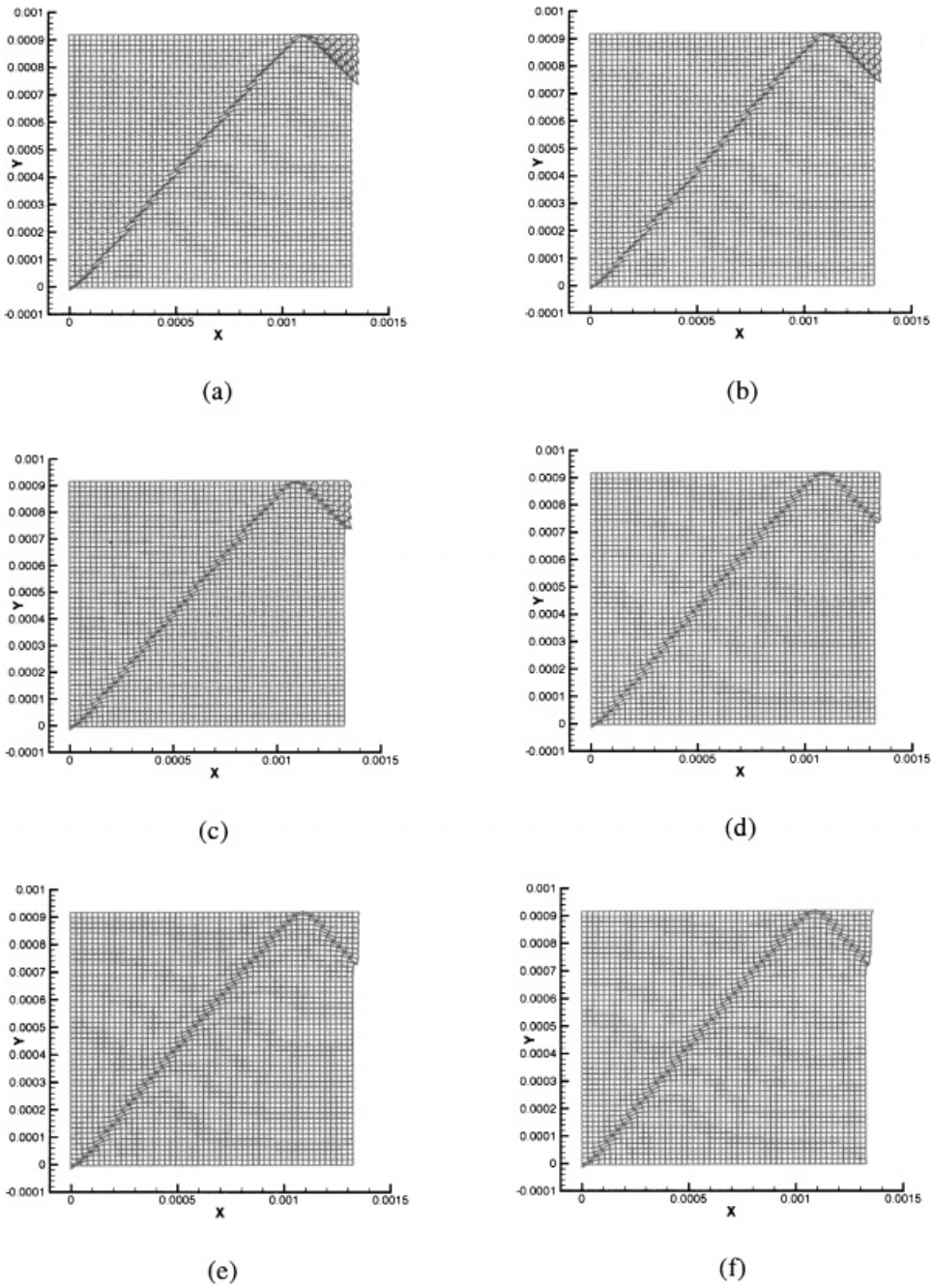

Figure 3. The mesh-free hour-glass control scheme: adjustment of dilation parameters a_x, a_y: (a) $a_x = a_y = 0.53$; (b) $a_x = a_y = 0.70$; (c) $a_x = a_y = 0.85$; (d) $a_x = a_y = 1.0$; (e) $a_x = a_y = 1.12$; and (f) $a_x = a_y = 1.2$.

specimen of a compressed slab. The computations have been carried out using 1-pt integration for regular RKPM shape functions with different support sizes, which is characterized by the dilation parameter, a_x, a_y. One may find that as the normalized dilation parameters, a_x and a_y, increase from 0.53 to 1.2, the undesirable hour-glass modes vanish in the process.

4.2. Special lumping technique

In explicit calculation, the row summation technique is often adopted to avoid the inversion of a large size consistent mass matrix, which not only offers computational convenience, but also provides reasonable frequency contents. In this study, we have found that different lumping techniques will produce different outcomes. In numerical experiments, two types of lumped mass are used in this study: (i) the conventional row-sum technique (see [21])

$$m_{ij} = \begin{cases} \displaystyle\int_\Omega \rho_0 N_i \, \mathrm{d}\Omega, & i = j \\ 0 & i \neq j \end{cases} \tag{64}$$

(ii) the 'special lumping technique' [34]:

$$m_{ij} = \begin{cases} \alpha \displaystyle\int_\Omega \rho_0 N_i^2 \, \mathrm{d}\Omega, & i = j \\ 0 & i \neq j \end{cases} \tag{65}$$

where

$$\alpha = \frac{\displaystyle\int_\Omega \rho_0 \, \mathrm{d}\Omega}{\displaystyle\sum_{I=1}^{\mathrm{NP}} \int_\Omega \rho_0 N_I^2 \, \mathrm{d}\Omega} \tag{66}$$

The justification of Hinton's special lumping technique is that it retains the diagonal part of the consistent mass matrix, and assumes that the diagonal part of the consistent mass matrix covers the correct frequency range of the dynamic response, whereas the non-diagonal part of the consistent mass matrix is not essential for the final results, or at least not in quasi-static cases. This technique ensures the positive definiteness of the mass matrix, and eliminates the singular mode. A possible setback could be that it cuts off the connection, or interaction between the neighbouring material particles. However, this setback may be compensated by the non-local nature of mesh-free methods, because each material point in mesh-free methods is covered by more than one shape function; therefore the interaction between the adjacent particles is always present. As a matter of fact, in our 2-D calculation, as many as 16 to more than 100 particles share their influences on the movement of a single particle; in the 3-D case, as many as more than 300 particles could be within the domain of influence of a single particle.

In numerical experiments, we simulate the tension test with both the row-sum lumping technique and the special lumping technique. In the particular test shown in Plate 5, two types of imperfection are planted in the tensile bar: (1) geometric imperfection: a reduction of the width of the tensile bar with the maximum reduction, 5 per cent at the middle cross-section; the tension specimen; (2) yield stress reduction, a distributed reduction of yield stress centred at the middle of the specimen. In this case, two sets of shear bands will be triggered by different sources of imperfections. The

outcome of the numerical computation is dictated by the competition between these two sets of shear bands. From Plate 5, one may see that the row-sum lumped mass solution predicts the shear band formation due to the reduction of yield stress well, and only leave a hardly noticed trace of another set of shear bands, which is due to geometric imperfection, in the background whereas for the numerical results obtained from special lumping technique, the two sets of shear bands are equally emphasized, and a great deal of detailed resolution is captured in the numerical solution. Apparently, combining the reproducing kernel interpolation with special lumping technique can provide high-quality, detailed resolution shear-band solution in numerical simulations. A high-resolution shear-band in a slab under compression is shown in Plate 6; it is interesting to note that the detailed pattern of the effective plastic strain contour seems to resemble the 'patchy slip' pattern in crystals [35].

5. ADAPTIVE PROCEDURES

In this section, some adaptive procedures, which are used to seek the refinement of the numerical solutions, are discussed. The attention here is focused on the two different types of adaptive procedures: *h*-adaptive refinement and a spectral-adaptive (wavelet) refinement.

5.1. h-adaptive procedure

The *h*-type refinement procedure has been used to capture shear-band formation for quite a while, notably, by Ortiz *et al.* [36], Belytschko *et al.* [37] and Zienkiewicz *et al.* [38] . However, technical difficulties have remained in the context of explicit finite element method. The commonly used Delaunay triangulation will certainly destroy the much needed quadrilateral (or hexahedral) pattern, and consequently the refined mesh is not suitable for explicit calculation anymore, though there is a recent attempt to store the triangle (or tetrahedra) element in explicit computation (see [39]); nevertheless, triangle element mesh is highly mesh-alignment-sensitive to the shear-band formation. On the other hand, mesh-free methods enjoy an amazing simplicity in the *h*-adaptive procedure. For the most part, one can just insert particles into the strain localization zone, and the subsequent numerical solutions will be automatically improved.

Since strain localization is a bifurcation problem in nature, elliptic adaptive indicators break down, a primitive or intuitive adaptive criterion is adopted here to determine where the adaptive region should be. We compare the effective plastic strain of every particle with that of its neighbouring particles, and choose those regions where particles with higher percentage of relative effective plastic strain to refine the numerical solution. This primitive adaptive index is fairly easy to implement and for the problems that we computed it works efficiently. It should be mentioned that a systematic study of mesh-free *h*-adaptive refinement in shear-band computation has been conducted by Jun and Im [40]. Some convergence issues have been addressed there, and we refer the readers to this recent study. To illustrate the *h*-adaptive procedure, a two-level, successive *h*-adaptive solution of a tension test is presented in Plate 7 and Figure 4. In the tension test shown in Plate 7 and Figure 4, the computation is carried out only in a quarter specimen by enforcing the symmetry conditions. In the zero-level run, 231 particles are used forming a uniform particle distribution in the specimen, which contains 200 background cells. In each cell, the 2×2 Gauss quadrature integration scheme is used. Based on relative effective plastic strain criterion, an automatic adaptive refinement procedure is implemented: at the first-level refinement, all the

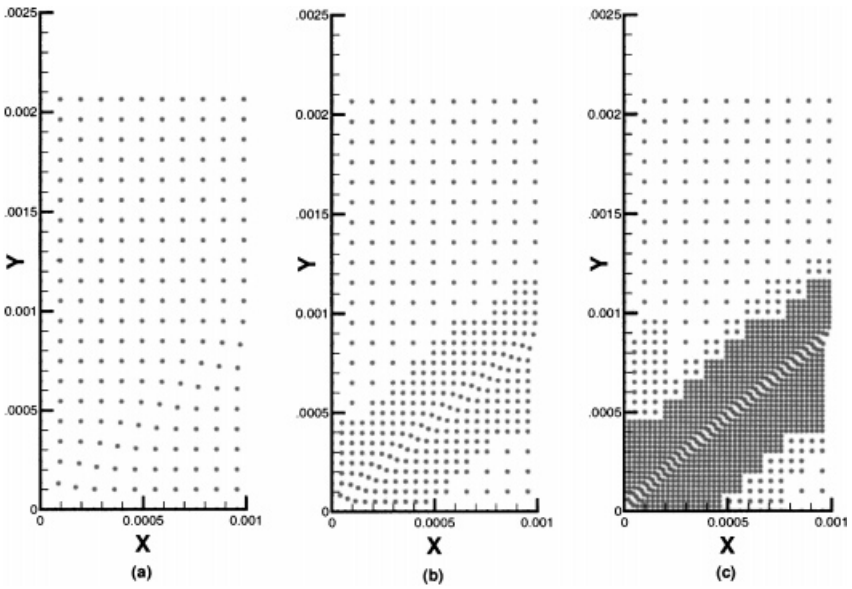

Figure 4. The shear-band formation in the tensile bar (only a quarter specimen is shown): (a) without any adaptivity; (b) the first-level adaptive solution; and (c) the second-level adaptive solution.

regions that have 25 per cent or more of relative effective strain are being refined, and the total number of particles increases to 429, with the corresponding 377 integration cells, which bring the quadrature points to 1508; at the second-level refinement, all the region that have 12 per cent or more of relative effective strain are refined, and the total particle number increases to 1264, and total quadrature points increase to 4664 respectively.

In order to explain why finite element approximation has difficulties in accommodating *h*-adaptive refinement in an explicit code, a simple illustration is demonstrated in Figure 5. If the above mesh-free discretization has a one-to-one correspondence with a quadrilateral mesh, one can set the fictitious connectivity map for each integration cell, as if they were individual elements. After a first-level refinement, we plot the deformed mesh in Figure 5; one can find immediately the entanglement and extrusion between the fictitious elements, which hints the break down of FE computation. Of course, in real FE approximation, this can only happen, provided that one can construct higher-order quadrilateral element along the boundary between coarse mesh and fine mesh.

5.2. *Spectral* (*Wavelet*)*-adaptive procedure*

Using spectral type of refinement to capture the localization mode can be traced back to the spectral overlay technique proposed by Belytschko *et al.* [41], which superposes a set of harmonic functions over the original FE shape functions at the place where shear band is supposed to develop.

In contrast to the spectral overlay technique, the adaptive wavelet algorithm proposed here is more general in nature. Instead of using analytical harmonic functions, we use the mesh-free hierarchical partition of unity outlined in Section 2, in which the higher-order spectral kernel functions are akin to the original RKPM shape functions. Intrinsically, the mesh-free hierarchical bases have a distinct distribution of spectral contents of the interpolating object among the different bases; in

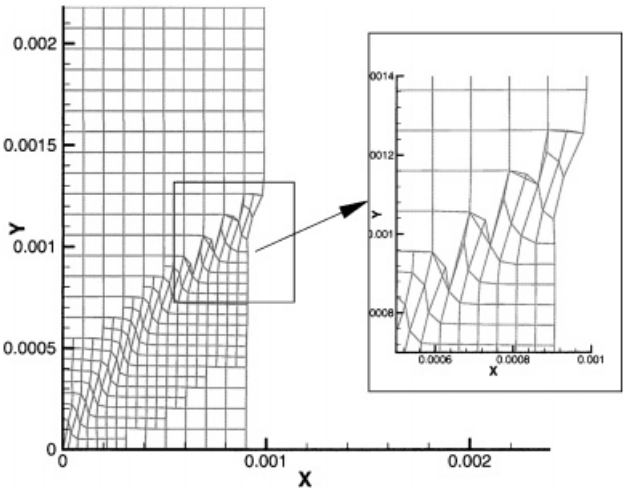

Figure 5. Why does FEM have troubles in *h*-adaptive refinement?

other words, they consist of a multi-spectral wavepacket. As a matter of fact, as shown in Reference [14], the higher-order basis functions do fit into the definition of the pre-wavelet function.[§] Furthermore, the orientation of the wavelet basis is isotropic in space, and the enhancement of the numerical solution due to wavelet basis comes out naturally as the outcome of numerical computation, though the adaptive regions are selected by a given criterion. Since the wavelet basis is genetically connected with the primary interpolation basis, the successive alternating *h*-*p* refinement processes may become possible.

Since the wavelet basis constitutes a partition of nullity, it introduces redundant degrees of freedom into the primary shape function basis. Consequently, the resulting stiffness matrix, and mass matrix will become ill-conditioned. In this study, we only use explicit integration scheme, and hence the only problem that we face is a possible singular mass matrix. As a matter of fact, the mass matrix will become singular, if the conventional row summation is used; and the mass matrix will become extremely ill-conditioned when consistent mass matrix is employed. To circumvent this difficulty, again we use the '*special lumping technique*' to form the mass matrix. Denote

$$\{\Phi_\ell(X)\} = \{\{\Psi_\ell^{[00]}(X)\}, \{\Psi_\ell^{[10]}(X)\}, \{\Psi_\ell^{[01]}(X)\}, \{\Psi_\ell^{[11]}(X)\}\} \tag{67}$$

By using the special lumping technique, one is always able to guarantee the positive definiteness of the mass matrix. The formula for mass matrix is given as follows:

$$m_{ij}^s = \begin{cases} \omega\delta_{ij} \displaystyle\int_{\Omega_X} \rho_0 \Phi_j^2 \, \mathrm{d}\Omega, & i = j \\ 0 & i \neq j \end{cases} \tag{68}$$

[§]By 'pre-wavelet', we mean that the admissible conditions for the basic wavelet function is satisfied.

where

$$\omega := \frac{\int_{\Omega_X} \rho_0 \, \mathrm{d}\Omega}{\left(\sum_{\ell=1}^{\mathrm{NP}} \int_{\Omega_X} \rho_0 \left(\Psi_\ell^{[00]} \right)^2 \mathrm{d}\Omega + \sum_{|\alpha|=1}^{\beta} \sum_{\ell=1}^{\mathrm{NAD}} \int_{\Omega_X} \rho_0 \left(\Psi_\ell^{[\alpha]} \right)^2 \mathrm{d}\Omega \right)} \tag{69}$$

However, there is a setback for this particular proposal. As one may find out, using the special lumping technique to avoid singular mass matrix will result in the increase of the total mass of a mass conservative system, i.e. an artificial added mass will flow into the system during adaptive procedure, since the added mass is proportional to the added degrees of freedom, or the wavelet shape functions. This could undermine the accuracy of the numerical computations, because of its non-conservative nature of mass. Nevertheless, based on our computational experiences, if the added degrees of freedom is less than 20 per cent of the total degrees of freedom, there is no obvious side-effect on numerical computations. Of course, a further evaluation may be necessary for precise assessment. A numerical tension test is conducted, and the results are plotted in Plates 8 and 9. Only geometric imperfection is planted in the specimen, as the reduction of the width of the tensile bar. The maximum reduction of the width of the tensile bar occurs at the middle cross-section, 10 per cent; then, it linearly varies along the x_2 direction back to the original width. From Plates 8 and 9, one can find that there is a significant improvement on the detailed resolution of the numerical solutions due to the wavelet refinement. Note that in Plate 9(c) the marked particles, i.e. the dark region, are the particles where the higher-order wavelet kernels are turned on. A separate account on wavelet-adaptive procedure on shear-band formation is presented in Reference [42].

6. SPECIAL TOPICS

6.1. Multiple shear-band/mode switching

As has been observed by Belytschko *et al.* [43], by changing the magnitude of induced imperfection in an elasto-viscoplastic material, the shear-band solution may change its pattern, or switch its mode, so to speak. This phenomenon may be attributed to the non-uniqueness of the non-linear bifurcation problem. So far for multi-dimensional problems, to the best of the authors' knowledge, there are few theoretical analyses available, if there are any at all, in studying such phenomenon. In reality and in computations, this is a typical bifurcation scenario where there are several different shear-band modes competing with each other; which shear-band mode will eventually dominate in the process, depending on many different factors, such as the strength of different types of imperfections, mesh or mesh-free discretization, or even the differences in mass lumping techniques, which has been shown in the previous sections.

Because of the complex nature and the charming appearance of the multiple shear bands, it is more often a pleasant experience of self-entertaining than the scientific curiosity to observe them in numerical computations. Nevertheless, this phenomenon is often difficult to be observed in finite element simulations, unless the finite element mesh is fine enough to have the adequate resolution. In contrast to the finite element method, the mesh-free RKPM interpolant is embedded in a highly smooth window function, and thus it may serve as a high-quality filter, which enable us to obtain high-resolution solutions with relatively coarse particle distribution.

In the previous computation done by Belytschko *et al.* [43], only a quarter of compression specimen, 1.0×1.0 mm, is computed with a 128×128 finite element grid. By changing the parameters of the yield stress reduction formula

$$\sigma_Y(x, y) = \bar{\sigma}_Y[1.0 - \gamma \exp\{-[(x_1 - x_{10})^2 + (x_2 - x_{20})^2]/r_0^2\}] \tag{70}$$

with parameter $r_0 = 0.1$, 0.0039, 0.00195 mm, three different shear-band patterns are observed.

We repeated the same calculation for a full-size compression specimen, 2.4×2.0, mm, in a 121×101 particle distribution; three distinct shear-band patterns have been observed for three different values of r_0 (Plates 3 and 10), i.e. $r_0 = 0.1$, 0.0041, 0.003 mm; the computations are done with the row-sum lumped mass.

The employed RKPM shape functions is constructed by a cubic-spline window function, and it can reproduce the polynomial basis $\mathbf{P}(\mathbf{X}) = \{1, x_1, x_2, x_1x_2\}$ exactly. Compared to the finite element calculation, the reproducing kernel particle method uses only one-fourth of the degrees of freedom that the finite element computation used, and obtains very sharp shear bands with distinct structures.

6.2. *Three-dimensional simulations*

The numerical simulations of shear-band formation in 3-D space is not an easy task for finite element methods. There are only few documented results in literature on 3-D shear-band simulation [27, 28, 44]. The main reason for this is the difficulty in special mesh design of a 3-D object. In our opinion, the best 3-D shear-band simulation is the one using brick (hexahedral) element with 1-pt integration/hour-glass control scheme [28], which, as elaborated earlier, has difficulties for *h*-adaptive refinement, and how to choose proper hour-glass control parameter is also debatable. Because of the lack of robust numerical interpolation scheme in 3-D case, high-quality shear-band solutions are usually difficult to obtain, which, to some extent, impairs the understanding of the three-dimensional shear-band structures.

The computation has been done for tensile bars with rectangular cross-sections, which is illustrated in Figure 6. The numerical experiment has been conducted for a set of specimens with different aspect ratios between the width of the specimen, W, and the thickness of the specimen, t. As pointed out by both Zbib and Jubran [28] and Tvergaard [44], there are two distinct necking modes present in tension tests: the diffuse necking mode and the localized necking mode (shear-band), i.e. a narrow groove inclined to the cross-section of the tension specimen.

One of the features on 3-D shear-band structure obtained in previous study (e.g. [44]) is that as the ratio t/W increases the necking mode in tensile bars with rectangular cross-section shifts from the localized necking mode to diffused necking mode. The numerical simulations conducted by using mesh-free interpolant also strongly support this claim, as one can observe the transition process in Figure 7. Nevertheless, this process is not that simple. If one plots the contour of effective plastic strain, one may find that the localized necking mode does not completely disappear without trace as t/W exceeds $3/8$, as reported in Reference [44]. In our numerical experiments, there are strong traces of localized necking mode left after t/W approaches 1, as indicated in Plate 11. This result agrees, to certain degree, with the 3-D shear-band result presented in [28], though we suspect that the visible localized shear-band modes at aspect ratio $t/W = 1, 3/2$ in Reference [28] may be due to the presence of the residual hour-glass modes.

The RKPM shape function used in the computations is constructed on a tri-linear polynomial basis, $\mathbf{P}(\mathbf{X}) = \{1, x_1, x_2, x_3, x_1x_2, x_2x_3, x_3x_1, x_1x_2x_3\}$, and a three-dimensional cubic spline box

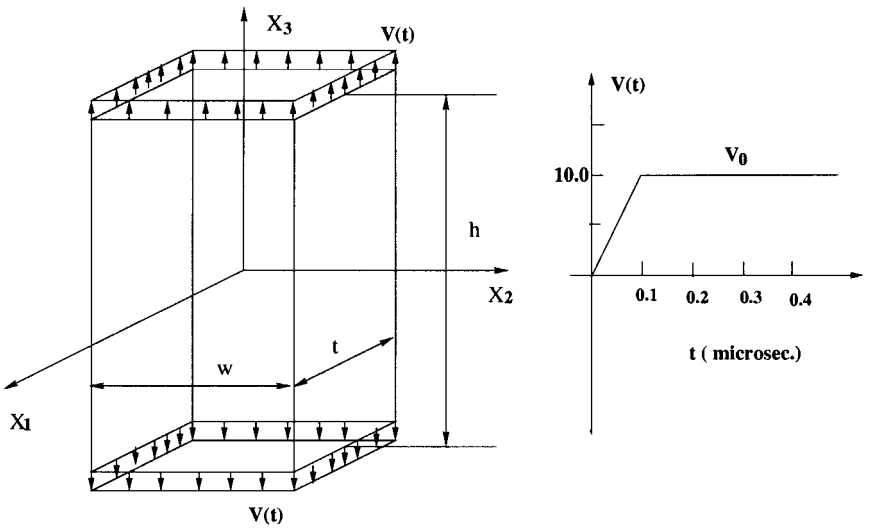

Figure 6. The tensile bar with rectangular cross-section.

function is embedded within the shape function to serve as the window function. In actual computations, a $2\times2\times2$ Gauss quadrature integration is used in each integration cell. Again as in the 2-D computation, we have not experienced any volumetric locking in the computation, which is based on a purely displacement-based explicit formulation.

7. CONCLUDING REMARKS

In this study, the reproducing kernel interpolants are used in a displacement-based explicit formulation to simulate shear-band formation in an elasto-viscoplastic material. The computations show that the mesh-free numerical algorithm developed here is viable, and robust in both 2-D and 3-D shear-band simulations.

The main advantage of using meshless methods in simulating shear-band formation is its simplicity. The best part of this approach is its ability to avoid volumetric locking while at the same time upholding certain 'mesh' or particle distribution objectivity in a simple explicit formulation, meaning that numerical results are independent of the particle distribution for a quasi-uniform particle distributions. Furthermore, the non-locality of mesh-free interpolation not only allows smooth discontinuous strain field, but also allows us to use '*the special lumping technique*' to produce high-quality, detailed resolution shear bands. In addition, the results presented here show that meshless discretization provides a favorable environment for *h*-adaptive refinement and by using the meshless hierarchical partition of unity proposed in Reference [18], a spectral (wavelet) adaptive procedure has been successfully implemented to refine shear-band solutions.

In the end, the authors would like to caution readers that the 'mesh alignment sensitivity' has not been completely eliminated in the mesh-free simulations, especially in the case of special lumping, or in the case where the particle density is not quasi-uniform. Nonetheless, the situations have been drastically improved compared with that of finite element methods. A complete eliminating

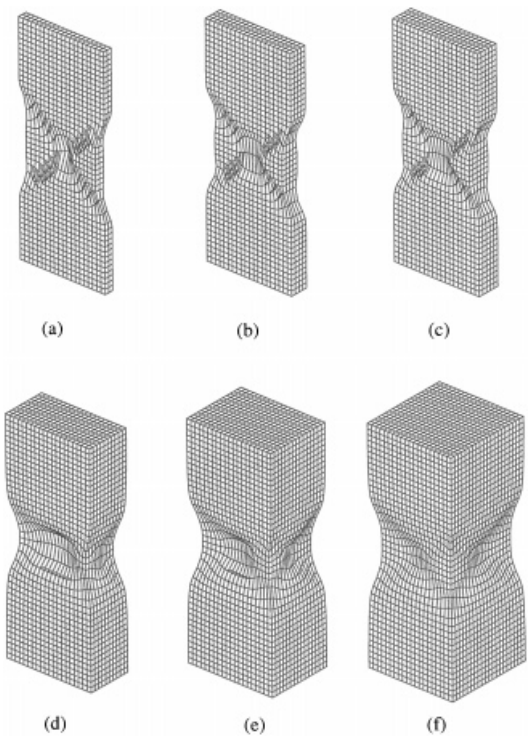

Figure 7. The shear-band formations in three-dimensional tension specimens with different aspect ratios between the width and the thickness: (a)$t/W = 1/10$; (b) $t/W = 1/5$; (c) $t/W = 14$; (d) $t/W = 1/2$; (e) $t/W = 3/4$; and (f) $t/W = 1/1$.

mesh-dependent sensitivities including mesh alignment sensitivity, as we speculated, would need a special Galerkin formulation designed for strain localization problems.

APPENDIX. THE ELASTO-VISCOPLASTIC SOLID GOVERNED BY POWER LAW

In this Appendix, the elasto-viscoplastic solid used in the computations is outlined. The chosen elasto-viscoplastic material is well regularized, at least in dynamic case, and the associated mathematical problem is well-posed as well. The shear bands, in this case, are due to the imperfection, or embedded inhomogeneities (see References [33, 37, 27]). The rate form constitutive equation reads as follows:

$$\overset{\nabla}{\boldsymbol{\sigma}} := \mathbf{C}^{\text{elas}}(\mathbf{d} - \mathbf{d}^{\text{vp}}) \tag{A1}$$

where the Jaumann rate of Cauchy stress, $\overset{\nabla}{\boldsymbol{\sigma}}$, is defined as

$$\overset{\nabla}{\boldsymbol{\sigma}} = \dot{\boldsymbol{\sigma}} - \mathbf{w}\boldsymbol{\sigma} + \boldsymbol{\sigma}\mathbf{w} \tag{A2}$$

and

$$\mathbf{d} := d_{ij}\mathbf{e}_i \otimes \mathbf{e}_j, \quad d_{ij} := \frac{1}{2}\left(\frac{\partial v_i}{\partial x_j} + \frac{\partial v_j}{\partial x_i}\right) \tag{A3}$$

$$\mathbf{w} := w_{ij}\mathbf{e}_i \otimes \mathbf{e}_j, \quad w_{ij} := \frac{1}{2}\left(\frac{\partial v_i}{\partial x_j} - \frac{\partial v_j}{\partial x_i}\right) \tag{A4}$$

A von-Mises-type viscoplastic solid is considered:

$$d_{ij}^{\mathrm{vp}} := \bar{\eta}(\bar{\sigma}, \bar{\varepsilon})\frac{\partial f}{\partial \sigma_{ij}} \tag{A5}$$

$$f(\boldsymbol{\sigma}, \kappa) = \bar{\sigma} - \kappa = 0 \tag{A6}$$

$$\bar{\sigma}^2 = \tfrac{3}{2}\mathbf{s} : \mathbf{s}, \quad s_{ij} = \sigma_{ij} - \tfrac{1}{3}\mathrm{tr}(\boldsymbol{\sigma})\partial_{ij} \tag{A7}$$

$$\bar{\varepsilon} := \int_0^t \sqrt{\tfrac{2}{3}\mathbf{d}^{\mathrm{vp}} : \mathbf{d}^{\mathrm{vp}}}\, \mathrm{d}t \tag{A8}$$

The power law that governs the viscoplastic flow is described as

$$\bar{\eta} = \dot{\varepsilon}_0 \left[\frac{\bar{\sigma}}{g(\bar{\varepsilon})}\right]^{1/m}, \quad g(\bar{\varepsilon}) = \sigma_0 \frac{[1 + \bar{\varepsilon}/\varepsilon_0]^N}{1 + (\bar{\varepsilon}/\varepsilon_1)^2} \tag{A9}$$

where m is the power index. This particular set of constitutive equations has been extensively used in shear-band calculation (see [28]), serving as a bench-mark-type constitutive model.

ACKNOWLEDGEMENTS

The authors would like to thank Mr. Gang Xue, who had participated in this work at an early stage. This work is supported by grants from the Army Research Office, and National Science Foundations. It is also sponsored in part by the Army High Performance Computing Research Center under the auspices of the Department of the Army, Army Research Laboratory cooperative agreement number DAAH04-95-2-003/contract number DAAH04-95-C-0008, the content of which does not necessarily reflect the position or the policy of the government, and no official endorsement should be inferred.

REFERENCES

1. Rudnicki JW, Rice JR. Conditions for the localization of deformation in pressure-sensitive dilatant materials. *Journal of Mechanics and Physics of Solids* 1974; **5**:875–887.
2. Tvergaard V, Needleman A, Lo KK. Flow localization in the plane strain tensile test. *Journal of Mechanics and Physics of Solids* 1981; **29**:115–142
3. Needleman A, Tvergaard V. Analysis of plastic flow localization in metals. *Applied Mechanics Review* 1992; **45**: S3–S18.
4. Needleman A. Material rate dependent and mesh sensitivity in localization problems. *Computer Methods in Applied Mechanics and Engineering* 1988; **67**:68–85.
5. Belytschko T, Lu YY, Gu. L. Element free Galerkin methods. *International Journal for Numerical Methods in Engineering* 1994; **37**:229–256.
6. Belytschko T, Krongauz Y, Organ D, Fleming M, Krysl P. Meshless methods: an overview and recent developments. *Computer Methods in Applied Mechanics and Engineering* 1996; **139**:3–48.

7. Liu WK, Jun S, Zhang S. Reproducing kernel particle methods. *International Journal for Numerical Methods in Fluids* 1995; **20**:1081–1106.
8. Liu WK, An introduction to wavelet reproducing kernel particle methods. *USACM Bulletin* 1995; **8**:3–16.
9. Liu WK, Chen Y, Jun S, Chen JS, Belytschko T, Pan C, Uras RA, Chang CT. Overview and applications of the reproducing kernel methods. *Archives of Computational Methods in Engineering*: *State of the Art Review* 1996; **3**:3–80.
10. Liu WK, Li S, Belytschko T. Moving least square reproducing kernel method part I: methodology and convergence. *Computer Methods in Applied Mechanics and Engineering* 1997; **143**:422–433.
11. Liu WK, Chen Y, Chang CT, Belytschko T. Advances in multiple scale kernel particle methods. *Computational Mechanics* 1996; **18**:73–111.
12. Liu WU, Chen Y, Uras RA, Chang CT. Generalized multiple scale reproducing kernel particle methods. *Computer Methods in Applied Mechanics and Engineering* 1996; **139**:91–158.
13. Monaghan JJ. An introduction to shp. *Computation Physics Communication* 1988; **48**:89–96.
14. Liu WK, Chen Y. Wavelet and multiple scale reproducing kernel method. *International Journal for Numerical Methods in Fluids* 1995; **21**:901–933.
15. Liu WK, Uras RA, Chen Y. Enrichment of the finite element method with reproducing kernel particle method. *ASME Journal of Applied Mecahnics* 1998; **64**:861–870.
16. Liu WK, Jun S. Explicit reproducing kernel particle methods for large deformation problems. *International Journal for Numerical Methods in Engineering* 1998; **41**:137–166.
17. Duarte CA, Oden JT. *Hp* clouds—an hp meshless method. *Numerical Methods for Partial Differential Equations*, 1996; **12**:673–705.
18. Li S, Liu WK. Reproducing kernel hierarchical partition of unity part I: formulation and theory. *International Journal for Numerical Methods in Engineering* 1999; **45**:215–288.
19. Chen JS, Wu CT. A generalized nonlocal meshfree method in strain localization. In *Modeling and Simulation Based Engineering*, Atluri SN, O'Donoghue PE. (eds). vol. 1. Tech Science Press: Palmdale, CA, 1998; 17–22.
20. Simo JC, Rifai MS. A class of mixed assumed strain methods and the methods of incompatible modes. *International Journal for Numerical Methods in Engineering* 1990; **29**:1595–1638.
21. Hughes TJR. *The Finite Element Method: Linear Static and Dynamic Finite Element Analysis*. Prentice-Hall: Englewood Cliffs, NJ, 1987.
22. Nemat-Nasser S, Chung D-T, Taylor LM. Phenomenological modelling of rate-dependent plasticity for high strain rate problems. *Mechanics of Materials* 1989; **7**:319–344.
23. Watanabe O, Zbib HM, Takenouchi E. Crystal plasticity: Micro-shear banding in polycrystals using voronoi tessellation. *International Journal of Plasticity* 1998; **14**:771–788.
24. Peirce D, Shih CF, Needleman A. A tangent modulus method for rate dependent solids. *Computers and Structures* 1984; **5**:875–887.
25. Chen JS, Pan C, Wu CT. Reproducing kernel particle methods for large deformation analysis of nonlinear structure. *Computer Methods in Applied Mechanics and Engineering* 1996; **139**:195–229.
26. Nagtegaal JC, Parks DM, Rice JR. On numerical accurate finite element solutions in the fully plastic range. *Computer Methods in Applied Mechanics and Engineering* 1974; **4**:153–177.
27. Tvergaard V. 3d-analysis of localization failure in a ductile material containing two size-scales of spherical particles. *Engineering Fracture Mechanics* 1988; **31**:421–436.
28. Zbib HM, Jubran JS. Dynamic shear banding: a three-dimensional analysis. *International Journal of Plasticity* 1992; **8**:619–641.
29. Ortiz M, Leroy Y, Needleman A. A finite element method for localized failure analysis. *Computer Methods in Applied Mechanics and Engineering* 1987; **61**:189–214.
30. Steinmann P, Willam K. Performance of enhanced finite element formulations in localized failure computations. *Computer Methods in Applied Mechanics and Engineering* 1991; **90**:845–867.
31. Simo JC, Oliver J, Armero F. An analysis of strong discontinuities induced by strain-softening in rate-independent inelastic solids. *Computational Mechanics* 1993; **12**:277–296.
32. Batra RC, Stevens JB. Adiabatic shear bands in axisymmetric impact and penetration problems. *Computer Methods in Applied Mechanics and Engineering* 1998; **151**:325–342.
33. Kosloff D, Frazier GA. Treatment of hourglass patterns in low order finite element codes. *Numerical and Analytical Methods in Geomechanics* 1978; **2**:57–72.
34. Hinton E, Rock T, Zienkiewicz OC. A note on mass lumping and related processes in finite element method. *Earthquake Engineering and Structural Dynamics* 1976; **4**:245–249.
35. Peirce D, Asaro J, Needleman A. An analysis of nonuniform and localized deformation in ductile single crystals. *Acta Metallurgica* 1982; **30**:1087–1119.
36. Ortiz M, Quigley JJ. IV. Adaptive mesh refinement in strain localization problems. *Computer Methods in Applied Mechanics and Engineering* 1991; **90**:781–987.
37. Belytschko T, Tabbara M. H-adaptive finite element methods for dynamic problems with emphasis on localization. *International Journal for Numerical Methods in Engineering* 1993; **36**:4245–4265.

38. Zienkiewicz OC, Hung M. Localization problems in plasticity using finite elements with adaptive remeshing. *International Journal for Numerical and Analytical Methods in Geomechanics* 1995; **19**:127–148.
39. Zienkiewicz OC, Rojek J, Taylor RL, Pastor M. Triangles and tetrahedra in explicit dynamic codes for solids. *International Journal for Numerical Methods in Engineering* 1998; **43**:565–583.
40. Jun S, Im S. Multiple-scale meshfree adaptivity for simulation of adiabatic shear band formation. *Computational Mechanics*, 1999, to appear.
41. Belytschko T, Fish J, Bayliss A. The spectral overlay on finite elements for problems with high gradients. *Computer Methods in Applied Mechanics and Engineering* 1990; **81**:71–89.
42. Li S, Liu WK. Reproducing kernel hierarchical partition of unity part II: applications. *International Journal for Numerical Methods in Engineering* 1999; **45**:289–317.
43. Belytschko T, Chiang H-Y, Plaskacz E. High resolution two-dimensional shear band computations: imperfections and mesh dependence. *Computer Methods in Applied Mechanics and Engineering* 1994; **119**:1–15.
44. Tvergaard V. Necking in tensile bars with rectangular cross-section. *Computer Methods in Applied Mechanics and Engineering* 1993; **103**:273–290.
45. Pan J. Perturbation analysis of shear strain localization in rate sensitive materials. *International Journal of Solids and Structures* 1983; **19**:153–164.
46. Shawki TG, Clifton RJ. Shear band formation in thermal viscoplastic materials. *Mechanics of Materials* 1989; **8**:13–43.
47. Needleman A. Dynamic shear band development in plane strain. *Journal of Applied Mechanics* 1989; **56**:1–9.

